UNIVERSITAT DE BARCELONA

Final Degree Project

Biomedical Engineering Degree

Impact of substrate curvature on fibroblasts' architecture and function

Barcelona, 8th June 2022

Author: Laura Crivillé Tena

Directors: Aina Abad Lázaro

Jordi Comelles Pujadas

Tutor: Elena Martínez Fraiz

Acknowledgements

First of all, I would like to express my deep and sincere gratitude to my directors, Aina Abad and Jordi Comelles, for their patience, motivation and for guiding me and providing feedback throughout the whole project. Without them it would have not been possible to complete this project. Also, I would like to express my gratitude to my tutor Elena Martínez, for giving me the chance to perform this work in her laboratory.

I would like to extend my gratitude to all the Biomimetic systems for cell engineering group members for treating me like one more in the lab and helping me anytime I needed. Thanks to Angela, Núria, Maria, Daniel, Vero and Melika, you have made me feel part of the group all these months.

A big thank you to all my friends for their support all along these last months that have been so intense, you have been of great help.

Last but not least, I want to thank my parents, specially my mother, without whose support I would have not made it. Thanks also to my uncle, aunt and grandparents, for all the unconditional support you have shown me during all this hard year. Finally, I want to specially thank my grandfather Vicenç, who taught me to never give up. I know how much he would have supported me during these moths. This project is dedicated to him.

Abstract

In biological systems, form and function are inherently correlated. Despite this key link between cells and the topography of the environment in which they naturally reside, it has not been since only a few years ago that three-dimensional (3D) topographical features have started to be considered when performing cellular experiments *in vitro* to understand physiological and pathological mechanisms underlying cell-cell and cell-environment interactions.

One of these key features involved in the 3D architecture of natural tissues is curvature, which is found in most organs of our body, such as the small intestine, which has a particular topography based on a set of invaginations and protrusions. Recently, curvature has been implied as a cue directing several cellular processes and having an impact on cell behavior, but almost all the studies performed to the date have been carried out with substrates having a higher stiffness than physiological tissues, and they were fabricated with quite complex methods. Moreover, most studies have focused on nanofeatures or cell-scale topographies, leaving macroscale curvatures such as those of the rete ridges in skin or of the crypts and villi in the intestine largely unexplored.

This is why in this project, taking as a reference the curvatures of the small intestine, soft hydrogel scaffolds have been fabricated by means of light-based 3D printing, a relatively simple and fast technique. The hydrogels contained convex, concave and no curvatures with different sizes in order to obtain distinct curvature ranges. During scaffolds functionalization, collagen reached all heights for convex curvatures, whereas on invaginations collagen did not retrieve the deepest ones, thus limiting their depth to 150 μm. Afterwards, NIH-3T3 fibroblasts have been seeded on these scaffolds and immunostainings for different cell markers have been performed in order to assess their expression levels and evaluate possible changes due to the different curvatures. The expression of YAP, laminin, α-SMA and vimentin has been found to differ significatively with changes in substrate curvature. Altogether, these results reveal that macroscale curvatures resembling the intestinal villi and crypts affect different cell processes including cytoskeleton organization, transcription factors localization and extracellular matrix (ECM) protein secretion.

This project has been ideated as a preliminary study to observe whether curvature-dependent changes are taking place, and therefore check if it would be worth extending the research to other cell types with higher complexity.

To all the people in Ukraine who have stood up for freedom. Because there is no progress without science, but there is no future without peace.

"Big wheels roll through fields where sunlight streams, meet me in a land of hope and dreams."

- Bruce Springsteen

TABLE OF CONTENTS

1. INTRODUCTION

1.1. Project context

Traditionally, cell-based assays have been carried out on two-dimensional culture surfaces, ignoring the three-dimensional nature of the tissue environments surrounding the cells. However, the development of cell-culture platforms that resemble as much as possible real physiological environments has taken increasing relevance in the last years. These efforts, which aim to better understand both physiological and pathological cellular processes, include reproducing the specific characteristics of the topography of native tissues. In particular, one of the features that affects the cells behavior is the curvature that they experience within the tissue. Actually, natural structures have roundish shapes which can be characterized by their curvature. This is also true for most of the tissues of the body, including the small intestine.

The small intestine is the longest organ in the gastrointestinal tract, being responsible for the absorption of nutrients, maintaining water and electrolyte balance, providing an immunologic barrier, and endocrine secretion. It is divided into three sections: the duodenum, jejunum and ileum *(1)*. The lumen is lined by the mucosa, which is composed of three distinct layers: the epithelium, the lamina propria, and the muscularis mucosae. The epithelium has a very particular architecture made of invaginations (crypts) and evaginations (villi) that confer the small intestine a highly curved tissue *(1)*. Villi are a series of finger-like projections into the lumen, with a density of 20-40 villi mm^{-2}, 0.2-1 mm in height and 0.1-0.25 mm in diameter *(2)* that serve to increase the surface area of the intestine, thus maximizing nutrient absorption and enhancing digestion. They are composed of terminally differentiated cells, mainly enterocytes but also goblet cells and enteroendocrine cells *(3)*. At the base of the villi there are the crypts of Lieberkühn, a set of cavities of the intestinal mucosa 0.3-0.5 mm in depth containing stem cells and transit amplifying cells *(4,5)*. These crypt-cells are constantly dividing and differentiating into the other cell types that constitute the intestinal epithelium on their journey up from the crypt to the villus tip, leading to continuous renovation of the entire cell population.

Intestinal epithelial cells sit directly above the basement membrane, which is composed of a reticular collagen fibrils sheet and resident fibroblasts. There are different types of fibroblasts composing the lamina propria, which have different localizations and functions, being one of them the maintenance of the intestinal stem cells niche. Along the crypt-villus axis, there are different kinds of fibroblasts exerting different functions. For instance, in the crypt region there is a specific type of fibroblasts called intestinal subepithelial myofibroblasts or telocytes, which are known to secrete Wnt proteins which promote the proliferation of intestinal epithelial stem cells *(6)*. Since some years ago curvature was appointed as a feature able to affect cell behavior, we hypothesize that these differences in function between the different fibroblasts might arise from the different curvatures within the invaginations and protrusions.

1.2. Objectives

The main aim of this project is to analyze and determine how the different curvatures on the substrate affect the cells lying on this topography. To achieve this goal, the following specific objectives will be pursued:

- To design different models of substrate curvature representing the crypts-villi microstructure of the intestine.
- To fabricate different hydrogels scaffolds reproducing the previously designed CAD (computer-aided design) models.
- To determine the role of substrate curvature in fibroblasts positioning and therefore observe if cell distribution varies with changes in curvature and how this takes place.
- To examine the impact of these curvatures on cell mechanics, that is, how uneven topographies alter cell adhesion and cytoskeletal architecture, and the resulting effects on the localization of transcription factors.
- To characterize the alterations in the secretion of extracellular matrix proteins on curved substrates, vital for the cells to carry out their functions adequately.

1.3. Structure

This section summarizes the overall structure of the project. Chapter 1 introduces the project and defines its objectives and the methodology. Chapter 2 is dedicated to review the background and the state of the art of the field, as well as making a brief description of the current bioprinting approaches and materials used to generate *in vitro* models. In chapter 3 we analyze the market perspectives, whereas in chapter 4 the current regulatory and ethical issues and the legal aspects are summarized. Chapter 5 exposes the different existing approaches for the project and discusses the selected solution, explaining in detail the chosen bioprinting technique and bioink, as well as defining all the tasks that have been carried out to develop the project and detailing the materials and methods necessary to pursue the experiments. Chapter 6 is dedicated to present, analyze and discuss the results obtained. The execution schedule followed to implement the project is detailed in chapter 7, and the technical and economic viability of the project are discussed in chapter 8 and 9, respectively. Finally, the conclusions and future perspectives of the project and the research field are exposed in chapter 10.

1.4. Methodology

In this section it is provided an outline of the methodology that has been followed to develop the project, which has been mainly based on experimental work. In addition, a review of scientific publications has been done to find out the state of the art of the field and the potential cell markers that could be used. Besides, the necessary data and information for the development of the several experiments have been obtained from previous work and protocols developed by the laboratory group. Briefly, the experiments consisted of first designing several models mimicking intestinal curvatures and optimizing the printing conditions to fabricate the hydrogels, in order to later seed the fibroblasts and, by means of the immunostainings of different markers, analyze the effects of the substrate curvature on the cells' behavior.

2. BACKGROUND

2.1. Translation from 2D to 3D

Nowadays, most current cell-based assays rely on two-dimensional (2D) monolayer cellular cultures. However, our organs have 3D complex structures that are indispensable for the function of that organ. That is why it has become so necessary, now that advances in technology allow the fabrication of 3D microstructures, to study cellular processes in an environment that resembles as much as possible, including the dimensionality and topography, the human physiology by developing microarchitectures that lead to reproduction of processes that take place in native tissues and organs.

For example, recent studies of cancer-cell behavior on planar substrates have suggested that interfacial geometry is an important factor in tumorigenicity *(7)*, but this corresponded to an in-plane curvature and line-tension effect imposed by geometric confinement and did not reflect the 3D architecture of tissues *(8)*. Similarly, there is accumulating evidence indicating that cells may respond differently when situated in 2D or in 3D mechanical microenvironments, where cells naturally reside *(9,10).* As an example, the focal adhesion (FA) composition and function of fibroblasts encapsulated in a 3D matrix were significantly different from those on 2D substrates *(11).*

Therefore, adequate 3D cues allow cells to exhibit more authentic functions when compared to traditional 2D cell cultures. *(12)* This can have especial relevance for instance in the case of drug screening. Orally administered drugs are mainly absorbed in the small intestine, so reliable *in vitro* intestinal models as a tool to engineer drug uptake and assess toxicity are needed. The ones already existing, scalable to industrially relevant numbers, have been restricted to only 2D monolayers of a human colorectal carcinoma cell line (Caco-2) cultured on standard *Transwell* inserts. Although this system has provided important biological insights at the same time of being simple and robust, they fail to recapitulate the complex 3D microenvironment of the small intestine, with the associated limited predictive value of drug uptake and transport. *(13)*

So, all in all, it has been shown that also for the case of the intestine, being a highly complex organ with a very specific microarchitecture, 2D intestinal models cannot precisely recapitulate biomimetic features *in vitro* and thus are unsuitable for various pharmacokinetic applications, development of disease models, and understanding of the host-microbiome interactions. As the complexity of the standard cell-based assays is not enough to recreate the real intricacy of the living systems, recent efforts have been directed toward recreating *in vitro* models with intestine-associated unique 3D crypt-villus architecture *(14)*. These novel approaches are characterized by accounting for the roundish shapes of the intestinal architecture. Interestingly, these curved surfaces, which contain concavities and convexities, may be more than a passive landscape and might have an actual impact in cell behavior.

2.2. Curvature effect

2.2.1. Cells positioning, migration and alignment

Recently, curvature has been implied as a cue to direct cell positioning in several cell types *(15).* In particular, adherent cells like mesenchymal stem cells (MSCs) and fibroblasts, responded to sinusoidal surface topography by positioning their nucleus close to topographical minima. MSCs response decreased with surface amplitude, and by exploring their surroundings while maintaining their nucleus in the most concave areas, they moved from one minima to another during their migrations. This phenomenon has been coined as *Curvotaxis.*

The influence of curvature on cell alignment was also demonstrated in *Bade et. al. 2017 (16),* where in a model of fibroblasts, isolated cells aligned strongly in the axial direction on glass cylinders with radii similar to the cell length whereas on cylinders of much larger radius, they partially lost this alignment *(16)*. In another study using "sphere-with-skirt PDMS surface", cells migrating on skirts repolarized to migrate in the azimuthal direction (Fig. 1). *(17)*

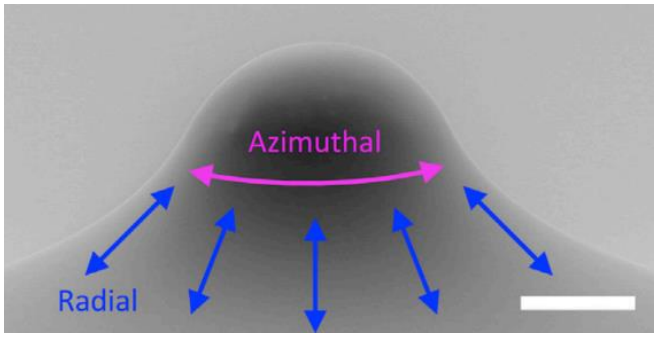

Figure 1: "Sphere-with-skirt" structure with radial and azimuthal directions. Scale bar 50 µm. Adapted from Bade et al. 2017. (16)

2.2.2. Cell morphology and architecture

Regarding cell morphology and architecture, *Pieuchot et. al. 2018*. *(15)* also found that nuclei of MSCs positioned on concave surfaces became more spherical than those cultivated on flat topography, whereas their average volume remained constant. This difference in nuclear shape suggests that cell positioning on concave curvatures leads to a mechanical relaxation of the nucleus. When cells are in a concave region, the adhesions are more elevated, and the stress fibers, which are connected to the substrate through the adhesions, might not compress the nucleus as much as on flat surfaces. In fact, they observed that cells positioned in convex regions exhibited short-lived and less-tensed focal adhesions (FA), whereas those that had anchoring points to concave areas were subjected to higher intracellular tension and thus were more stable. Following with the morphological changes in this cell type, *Lee et. al. 2017* cultured hMSCs on polyacrylamide (PAA) gels with embedded micro glass balls (Fig. 2) to study how affected the cell spreading. They found out that in contrast to the well-spread morphologies growing on flat glass plates, cells' morphology growing on the glass balls was almost uniformly spindle-shaped. *(18)*

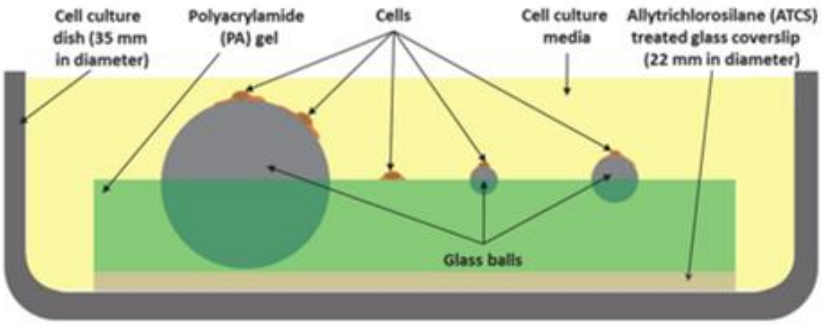

Figure 2: PAA gel with embedded glass microballs to study the effect of curvature on cell spreading. Adapted from Lee et al. 2017. (18)

In another study, significant reconfiguration of two subpopulations of stress fibers was shown when fibroblasts were exposed to non-zero Gaussian curvature (the product of the substrate curvatures) seeded on sphere-with-skirt polydimethylsiloxane (PDMS) surface. (Fig. 1) Apical stress fibers in cells on skirts aligned in the radial direction and avoided bending by forming chords across the concave gap, whereas basal stress fibers bended along the convex direction *(17).*

In a study regarding kidney tubules' curvature, *Yu et. al. 2018* cultured two types of renal epithelial cells (Madin-Darby canine kidney cells (MDCK) and human kidney 2 (HK-2)) on a microchannel with a broad range of curvatures made of PAA gel (Fig. 3) and found out that cellular architecture on curved substrates was closely related to the cell type-specific characteristics and the sign and degree of curvature. As the curvature increased on convex channels, HK-2 aligned their in-plane axis perpendicular to the channel but did not change significantly in morphology. On the other hand, MDCK cells, having higher stiffness, showed minimal change in both morphology and alignment. However, on concave channels, both cell types were elongated and showed longitudinal directionality, although changes in MDCK were more conservative. Furthermore, substrate curvature contributed to cell polarization by enhancing the expression of apical and basolateral cell markers. *(8).*

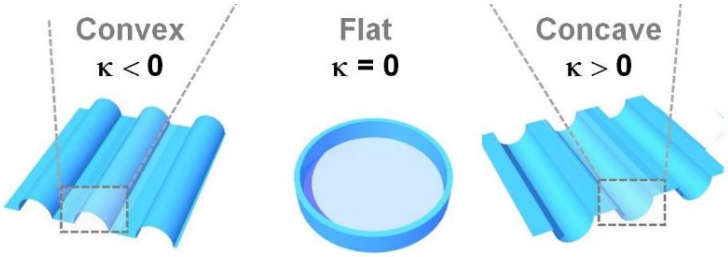

Figure 3: Schematic diagram of PAA gel microchannels fabricated to study the effect of curvature on renal epithelial cells. Adapted from Yu et al. 2018. (8)

2.2.3. Gene expression and transcription factors

Curvature has also been proved to have effects on cells gene expression. *Pieuchot et al. 2018 (15)* found out that substrate curvatures had different effects on hMSCs transcriptome by comparing cells cultivated both on flat (control) and sinusoidal surfaces. 637 genes being differentially regulated were identified, from which 361 had biologically described functions. Among them, genes

involved in response to stress, cytoskeleton remodeling and cell proliferation were the most downregulated. However, some upregulated genes were also found, mainly related to ECM remodeling. Moreover, *Lee et. al. 2017* performed an RT-PCR analysis which revealed that the substrate curvature alone can induce adipogenesis of the hMSCs *(18).*

Additionally, curvature has been proved to play a key role in cell reprogramming too. *Sia et al. 2016* were able to improve efficiency of reprogramming fibroblasts to cardiomyocytes by culturing the cells on microgrooved substrate, which enhanced the expression of cardiomyocyte genes and improved the yield of reprogrammed cells *(19).*

Altogether, substrate curvature impacts cell positioning, migration and alignment, plays an important role to modulate the cellular morphology and phenotype, and it is involved in regulating gene expression and differentiation.

2.3. Crypt-villi microstructures

As explained before, the small intestinal tissue has a particular topography based on crypts and villi leading to roundish curvatures which is aimed to reproduce. Along the years, several methods that lead to the fabrication of substrates with crypt-villus architecture have been published. Below we review the most important ones.

A first approach was performed by *Sung, et al. 2010*, who employed a method combining laser ablation and sacrificial molding techniques to fabricate hydrogels into 3D geometries with high aspect ratio and curvature (Fig. 4). First, laser ablation created a controlled array of deep holes in a plastic mold. This primary mold was then used to make a secondary PDMS mold with the desired features. The PDMS mold was then used to create a sacrificial mold made of calcium alginate, which was dissolved after forming a 3D structure with the final hydrogel. With this method, they obtained a collagen scaffold mimicking the 3D geometry of the gastrointestinal tract villi *(12).*

Wang et. al. 2017 developed a micropatterned collagen scaffold to generate in vitro human small intestinal epithelium. Besides the key features of crypt-villus architecture, this scaffold had a suitable extracellular matrix and a physiological stiffness. Briefly, PDMS stamps were produced from master molds with the desired features and then commercial Transwells were modified by substituting their polycarbonate porous membrane for a hydrophilic photo-patterned polytetrafuoroethylene (PTFE) membrane. Collagen scaffolds were micromolded and crosslinked on the surface of the PTFE membranes, and PDMS stamps were placed on top of the modified Transwells, and removed from the collagen scaffolds after pressurization under 40 psi nitrogen for 2 hours *(20).*

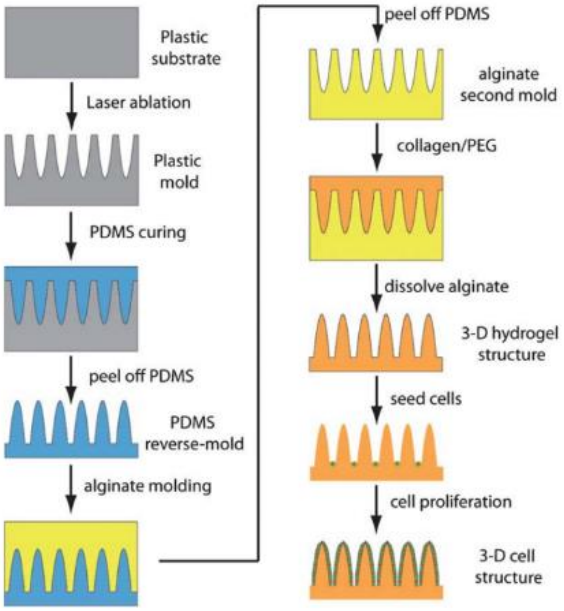

Figure 4: Fabrication of villi-like hydrogel from PDMS mold. Adapted from Sung, et al. 2010 (12)

A third approach is based on poly(glycerol sebacate) (PGS) scaffolds mimicking the villi architecture of the small gut *(Ladd, et. al 2019).* Using laser ablation, they created a template array of 500 mm deep, high aspect ratio holes on a polymethyl-methacrylate (PMMA) template, and from there PDMS was used to fabricate replicas of the final scaffolds with a full villus array, onto which molten agarose was poured *(21).*

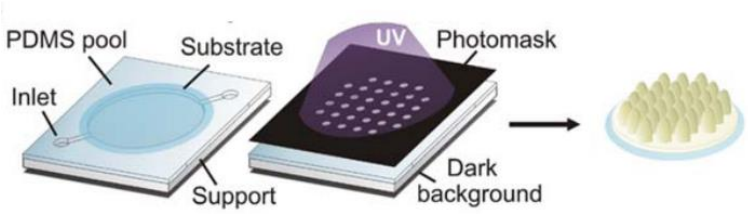

Figure 5: Fabrication of scaffolds by photolithography. Adapted from Castaño et al. 2018 (2)

Work performed previously in our lab by *Castaño et al. 2018* introduced great advantage by generating a mold-less approach to produce complex microstructures, allowing the fabrication of 3D intestinal tissue models by conventional photolithography. The method is based on the crosslinking of a photoresist through a 2D photomask with a desired pattern upon exposure to collimated UV light. (Fig. 5) By means of the modification of the Damköhler number (Da), which is the ratio of the characteristic oxygen diffusion to oxygen depletion times, different microstructures could be produced by exposing a poly(ethylene glycol) diacrylate (PEGDA)-acrylic acid (AA) solution to UV light in a MJBA Mask Aligner. When Da ~ 1, objects with conical shapes were formed, which mimicked the characteristic intestinal villi. Da was adapted by changing the distance to the polymerization light source. The villus-like micropillars were fabricated by placing patterned photomasks on top of glass coverslips or porous membranes and then the prepolymer solution was exposed for 60-220 seconds to UV light in a MJBA Mask Aligner *(2)*.

Finally, *Taebnia et. al. 2021* followed a similar procedure to print dual-material villi-wells, where the scaffolds were fabricated using a custom-built projection-based stereolithography printer. (Fig. 6) Hydrogels were made of PEGDA of different molecular weight and $PEGDA_{700}$ mixed with gelatin methacrylate (GelMA), which made the mechanical properties vary between hydrogels *(13)*.

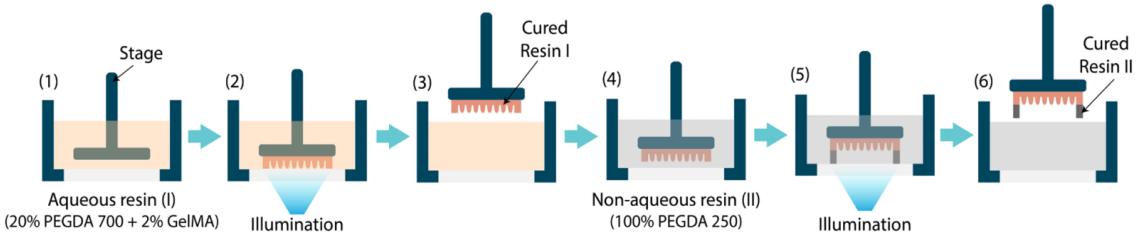

Figure 6: Printing procedure of PEGDA-GelMA hydrogels with stereolithography printer. Adapted from Taebnia, et al. 2021 (13)

2.4. Hydrogels

Until now, the studies addressing the effect of substrate curvature on cells behavior used materials which did not have the most appropriate mechanical and chemical properties when compared to in vivo tissues. Although the results are extremely insightful to understand the role of curvature in cell behavior, they might not be fully accurate since they do not reliably mimic the tissue environment. Other studies have proposed hydrogels as alternative cell culture substrates *(22–24),* as they have a broad range of mechanical properties which make them resemble much more soft tissue microenvironments (< 40 kPa).

Hydrogels are defined as 3D networks comprising crosslinked hydrophilic polymer chains, distinguished by their high-water content. Hydrogels can be designed and printed into a variety of shapes, sizes, and forms to meet the final product requirements, and can also be engineered to mimic the extracellular tissue microenvironment *(25)*. They can be natural or synthetic, being synthetized from natural or synthetic polymers respectively. Natural hydrogels have better biological properties than synthetic ones, but they suffer from some drawbacks such as poor mechanical and rheological properties, limited long term stability, and batch-to-batch variability. On the other hand, synthetic hydrogels are more tunable to provide the desired mechanical properties and degradation rates, though they are usually not biocompatible by themselves, so further modification to introduce cell-adhesive motifs is required *(26)*.
Alginate, hyaluronic acid, collagen, agarose, gelatin, polyethylene glycol (PEG) and its derivatives PEGDA, Poly(ethylene glycol) monomethacrylate (PEGMA),... are some examples of the most common used materials to fabricate hydrogel scaffolds for tissue engineering. Among these, PEG is a synthetic material formed by polymerization of ethylene oxide, highly valuable for its hydrophilicity that facilitates exchange of cell's nutrients and waste. Also, PEG-derived materials allow hydrogel to be photocrosslinked, which provides better mechanical stability after bioprinting. Particularly, PEGDA presents a high hydrophilicity, a bioinert structure, and a lack of toxic or immunogenic responses *(26)*.

Recently, stimulus-responsive hydrogels have increasingly gained scientific interest, being able to respond to stimuli like light, chemicals and temperature to induce structural or morphological transitions. Among them, light stimulus, for instance UV or visible light, is considered an ideal external control method to manipulate the properties of hydrogels due to their several advantages, including the abilities to: i) easily control the stimulus by switching the light on and off; ii) precisely regulate light dosage to achieve functional tunability; iii) obtain independent spatial or temporal control of different biological processes in a wavelength-specific manner; iv) direct light to a confined location at user-defined times; and v) regulate a range of cellular processes *in vivo* happening within the range where light has its maximum penetration in tissues *(27)*.

Materials	Major properties	Limitations
Glass	+ Surface stability + Optically transparent + Electrically insulating	- Not gas permeable - High cost of fabrication
PDMS	+ High elasticity + Biocompatibility + Rapid prototyping	- Hydrophobicity - Strong adsorption of biomolecules
Plastic	+ Optically transparent + Low absorption + Suitable for mass production	- Less gas-permeable - Unsuitable for prototyping
Collagen	+ Biocompatible + Enzimatically degradable + Similar to native tissues + Good cell adhesion	- Weak mechanical properties
Gelatin	+ Biocompatible + Biodegradable + Similar composition to collagen + Good cell adhesion + Tunable properties by addition of functional group (GelMA)	- Weak mechanical properties - Rapid degradation
Alginate	+ Biocompatible + Biodegradable + Easy functionalization	- Weak mechanical properties - Poor cell adhesion - Uncontrollable degradation
PEG and derivatives	+ Biocompatible + Tunable and precise mechanical and degradation properties + Relatively low protein adsorption + Low degradation rate + High resistance to swelling in aqueous environment	- Less cell adhesive (can be solved with addition of AA) - Limited biodegradation

Table 1: Comparison between different materials to fabricate in vitro models. Adapted from Choi et al. 2019 and Ding et al. 2020. (27,28)

2.5. Bioprinting approaches

Bioprinting is an emerging technology that provides high reproducibility and precise control over the fabricated constructs in an automated manner, potentially enabling high-throughput production. During the bioprinting process, a solution of a biomaterial is used to create tissue constructs *(29)*. 3D bioprinting offers great versatility to fabricate biomimetic, volumetric tissues that are structurally and functionally relevant. It enables precise control of the composition, spatial distribution, and architecture of resulting constructs facilitating the recapitulation of the delicate shapes and structures of targeted organs and tissues *(30)*.

A variety of 3D bioprinters have been developed all over the world by numerous companies. There is a wide variety of them in the market, but in order to be suitable for biomedical applications their main requirements are *(31)*:

- Affordable: everyday more and more researchers set food in this area, and devices with unreasonable prices would be a barrier for newcomers.
- Workable: an ideal printer should not be very complex to use and not too big either. With a modularized configuration users can select different modules according to their needs, while compact equipment allows printing within a standard bench.
- Quantifiable: standardization and consistency evaluation of printing process is needed. A quantitative standard of printing quality should be established both at the level of structure precision and cell growth.
- Applicable: cell injuries such as mechanical damage in printing process should be avoided.

Regardless of the specific technique on which is based the selected bioprinter, all of them follow these steps to achieve the desired construct *(32)*:

- Data acquisition: 3D models can be obtained using several imaging techniques (in the medical world would be X rays, magnetic resonance,...) or directly using computer aided design (CAD) software to program the desired model. These 3D models are then divided into 2D horizontal slices.
- Material selection: this step requires the election of the materials that will be used to fabricate the final construct. It can include cells, growth factors, hydrogels,... The combination of these materials is called bioink.
- Bioprinting: before printing the structure, appropriate configuration of the printing parameters needs to be confirmed, and observation of the results obtained with them is necessary along the process to make adjustments if required. Parameters might vary according to the technique and also the bioink used.

As mentioned before, there are several techniques on which are based the bioprinters to fabricate the 3D structures. The main ones used nowadays for biomedical applications are extrusion-based bioprinting, droplet-based bioprinting and photocuring-based bioprinting. (Fig. 7) *(31)*

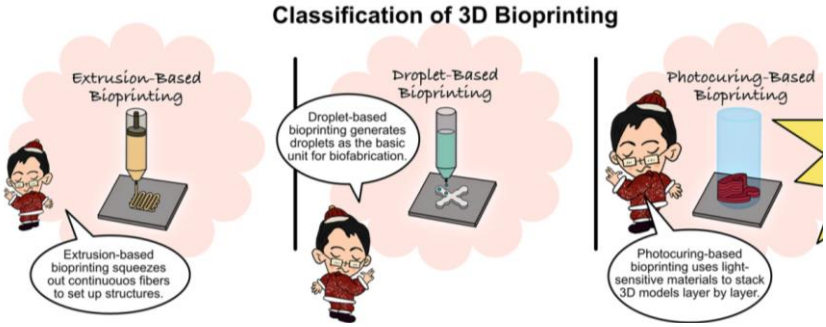

Figure 7: 3D bioprinting main techniques. Adapted from He et al. 2020. (31)

2.5.1. Extrusion-based bioprinting

This technique is the most widely used 3D bioprinting methodology mainly due to its versatility and affordability. *(32)* A bioink is extruded through a nozzle by means of mechanical or pneumatic driven force, which forms continuous microfilaments that are deposited on a substrate and finally stacked into the desired structure by the deposition of several layers. (Fig. 8) There are three main technologies according to the actuating modes of the dispensing system:

- **Pneumatic-driven extrusion**: it uses compressed air to release the liquid, usually with a bioink loaded syringe connected to an air pump. It requires sterilization of air from the air pump, and extra liquid or gel-based medium needs to be added in order to guarantee a smooth extrusion.
- **Piston-driven extrusion**: a piston is connected to a motor through a guide screw. Thanks to the motion generated when the motor is started, the bioink is pushed out of the nozzle by the mechanical force of the piston. This option is more suitable for extrusion of high viscosity biomaterials.
- **Screw-driven extrusion**: it is also based on a mechanical driven liquid dispense. It is similar to the piston-driven extrusion, but in this case the screw connected to the motor is directly used for extrusion instead of the piston, providing more pressure which might damage the bioink if for example it contains cells.

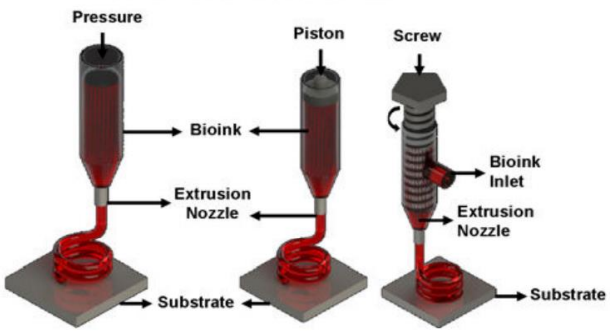

Figure 8: Principles of extrusion-based bioprinting. Adapted from Heinrich et al. 2019. (30)

In all the cases, parameters like temperature, nozzle diameter, extrusion pressure, movement speed, extrusion speed,... might influence the final bioprinted structures. Piston and screw-driven techniques provide a higher resolution and better printability with semi-solid or solid state biomaterials than pneumatic-driven method. However, they are volumetric limited, their cleaning and disinfection is much more complicated and they are more expensive.

2.5.2. Droplet-based bioprinting

Compared to extrusion-based bioprinting, this methodology has a higher resolution due to the fact that it uses independent and discrete droplets as a basic unit instead of continuous filaments. (Fig. 9) The use of single droplets makes it a simple technique and with high control of the deposited material. *(32)* It can be classified into three different methods:

- **Inkjet bioprinting**: it is based on two main steps: first, independent droplets are formed and directed to the desired substrate location, and then there is an interaction between the droplets and the substrate. It can be divided into two different techniques according to the principle used to form the droplets: Continuous Inkjet (CIJ) and Drop-on-Demand (DOD). CIJ has higher drop generating frequencies, whereas DOD works at lower frequencies but achieves smaller drop volumes allowing a higher printing resolution. Moreover, CIJ has several sterility issues which makes it inadequate for biological applications.
- **Electrohydrodynamic jetting (EHDJ)**: it uses an electric field, which avoids the excessive pressure on the bioink when it is extruded through the nozzle in inkjet printing. A metallic nozzle is filled with bioink until it forms a spherical meniscus, and then a high voltage is applied between the nozzle and the substrate producing the accumulation of ions at the meniscus. When electrostatic stresses overcome the surface tension of droplet this is ejected from the nozzle. The variation of voltage affects the size of the droplets.
- **Laser assisted bioprinting (LAB):** it is a non-contact, nozzle-free method, but it is the most complex within the techniques generating droplets. It uses a pulse laser to excite a bioink-coated ribbon structure, from which droplets are ejected towards a receiving substrate thanks to the evaporation and high-pressure bubbles formation due to the action of the laser on the absorbing layer of the ribbon structure.

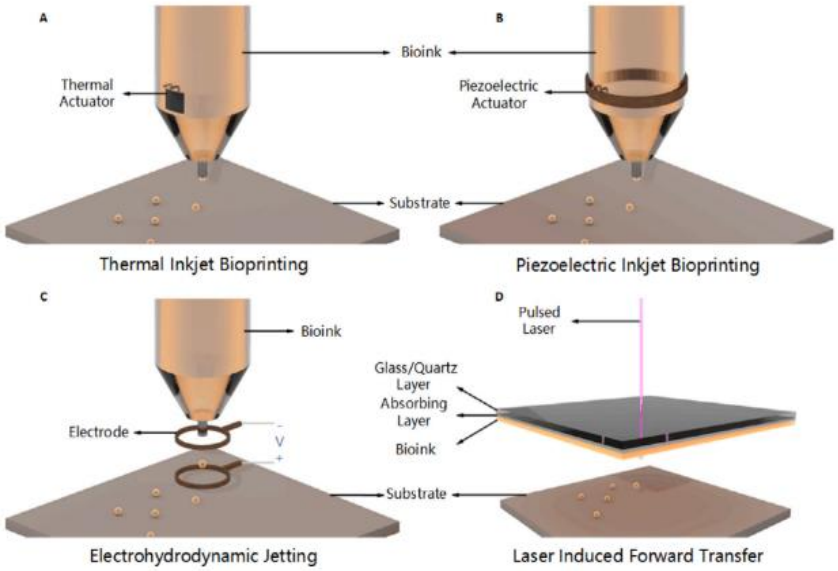

Figure 9: Principles of droplet-based bioprinting. Adapted from Gu et al. 2020. (32)

The fact of being a nozzle-free method allows LAB to avoid a series of issues such as cross-contamination, nozzle clogging, bioink damage,... and it also produces smaller droplets and has higher precision compared to the other two techniques. However, it requires a more complex system including a laser source and a quartz layer, leading to an increased cost and lack of availability.

2.5.3. Photocuring-based bioprinting

This bioprinting approach relies on the the photopolymerization of photosensitive polymers under precisely controlled light. (Fig. 10) According to the different light scanning modes, two different methods have been stablished *(32)*::

- **Stereolithography (SLA)**: the bioink is filled in a tank with a platform that moves up and down, so that when the first layer is printed the platform shifts to the surface of the bioink solution and the liquid solidifies upon exposure to a UV laser. This laser provides the energy that results into the formation of covalent bonds between adjacent polymer chains in the bioink. For each layer, the laser scans through a 2D pattern, and instead of focusing directly on the solution it reflects from a mirror to the appropriate point. By submerging the platform in the solution and moving it up a distance equal to the layer height, the last cured ink is attached to the previous layer, and by repeating this process the 3D structure is completed.
- **Digital light processing (DLP)**: in this case a complete layer is solidified at once instead of point-by-point, so after the first layer is printed the new layers are polymerized above the previous one. It is based on three components: a container filled with bioink that includes a photocurable hydrogel or photosensitive resin, a lifting platform ensuring the correct lowering at a certain height, and an imaging system. A dynamic mask is used in order to achieve the photocuring of one complete layer at once: it carries a design pattern through which light passes and transmits the pattern to the receiving substrate.

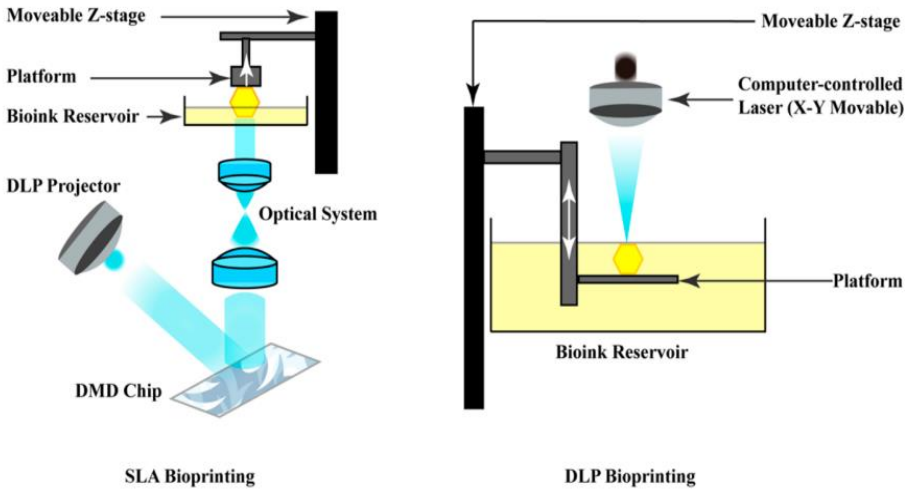

Figure 10: Principles of photocuring-based bioprinting. Adapted from Liang et al. 2021. (33)

Although in both cases the construct is printed upon light exposure, the fact of printing one layer at once instead of point-by-point like in SLA makes DLP a much faster process no matter the complexity of the structure. Besides, in SLA, excess of bioink needs to be cleaned, and factors such as laser power, scanning speed, exposure time, laser spot size,... might determine its precision.

2.6. Generation of knowledge

As it has been explained, substrate curvature has been proved to affect the cells' behavior in several ways such as positioning and migration. However, most of the studies performed to the date studying these effects have used substrates with stiffness higher than physiological tissues, and they were fabricated with quite complex methods requiring many steps. For instance, in the work performed by *Pieuchot et al. 2018 (15)* that has been previously exposed, the substrate curvatures were designed in a two-step electrochemical process consisting of a mask electrochemical micromachining to first create the 3D preforms, and then a smoothening by mass transport-limited dissolution. Once the stainless steel molds were fabricated with the desired topography, the final substrates were obtained by replica molding with PDMS. Other materials that have been typically used in more studies are glass or silicon among others, which all are stiffer than biological tissues.

In the present project we address the effect of curvature on cells using soft hydrogels as substrate, having a stiffness that resembles much more the physiological one, and made of a bioink that has not been tested previously in this area of study. Also, the technique used for the fabrication of the hydrogels is a moldless approach with enough resolution to mimic anatomical curvatures and with a customized printer developed by the members of the laboratory. Moreover, the cell type for this project is a fibroblast line, whereas most of the studies addressing this subject have performed experiments with epithelial cells. With this it is aimed to contribute in the field of cell interaction with substrate topography, taking increasing relevance in the research to generate biomimetic environments for cell biology studies or tissue engineering and organoids.

3. MARKET ANALYSIS

Nowadays, with the increase in global population and the lengthening of life expectancy, increasing the number of pathologies that might lead to the need of organ transplant, it has augmented the concern of not being able to cover the high demand for organ transplantation. In fact, this high market demand can be easily seen just by looking at the United States organ shortage crisis, though it is one of the countries where major advances on the field are being done. On average, 22 people die every day while awaiting an organ transplant. The waitlist for organs is over 116,000 people long and, every 10 minutes, someone new is added. Over the last 5 years, the number of organ transplants has increased by 20%, hitting a new record of over 33,500 transplants in 2016 *(34)*. Clearly, the organ supply will not catch up with the current demand without some assistance from another source such as 3D printers that can manufacture organs.

Experts estimate the value of the 3D bioprinting market alone to be in the hundreds of millions of dollars already. Furthermore, the market is growing at an annual rate of approximately 44%, which puts market value estimates in billions within few years. More broadly, in 2018 26% of manufacturing companies had already invested in 3D printing globally and that number is projected to climb almost to 60% by 2022. The health care sector could benefit from following the manufacturing sector's example because productivity in this sector has increased 78% in the last fifteen years, while the health care sector has essentially remained stagnant at just 6% during that time. *(34)* Industry reports note a list of important factors that currently act as growth driving forces for bioprinting, including the aging population, the desire to move away from animal testing, clinical needs for wound care, and the continued improvement of the bioprinting field, among others, and also the promise to be a substantial money saver for many players.

There are already many companies who trust in the potential of this technology and its utilities that are trying to develop fully functional engineered tissues and organs, and materials and technologies to achieve it. The two leading companies at the moment that should be remarked are Organovo (San Diego, California, USA) and Cellink (Boston, Massachusetts, USA) The first one has been developing a line of human tissues for use in medical research and drug discovery, which include both normal tissues and specially designed disease models. They are also working on specific tissues for use in clinical patient care. Actually, in 2014 they announced the successful printing of hepatic tissue that worked as a real liver for several weeks. Organovo also made a research partnership with L'Oréal to achieve the development of synthetic skin. Cellink, on the other hand, is focusing its work on developing bioprinters, bioinks, high biocompatible materials and all the technologies necessary for developing all the organ models and engineered tissues stated before. Actually, focusing more on our project englobed in intestinal tissue models, this company performed an experiment with a novel printer and ink developed by them (*CELLINK EPI X* ink using the *CELLINK BIO X* printer) in which they evaluated the viability of Caco-2 cells after being bioprinted. The results showed that cell number and viability in 3D-bioprinted constructs remained stable between days 1 and 8. All analyzed samples exhibited over 80% viability.

So, all in all, large companies are starting to show interest for these technologies and are investing in research departments to try to develop in vitro lines of human tissues that can work like biological

ones. These advances prove the high potential of organoids technology and reaffirm the utility and the need of investment in these research lines due to the great future perspectives. Indeed, both industry and world leaders have already recognized the potential and opportunities behind this research and novel technology. Former United States president Barack Obama said *"3D printing has the potential to revolutionize the way we make almost everything." (34)* So medicine should not be an exception. In fact, both the bioprinting community and the pharmaceutical industry have taken great interest in the promise of 3D printed organs. Start-up companies committed to this area have emerged and survived, and American pharmaceutical giants such as Johnson & Johnson have taken notice. With future economic projections in the billions, and industry giants from various sectors on board, 3D printing is here to stay.

Regarding this project, although it is a research work at academic level, and a little grain of sand to the great perspectives opening in the world of 3D bioprinting and organoids design, all these discoveries and knowledge once tested and approved could be then transferred to corporations in order to fabricate organoids and other similar products such as *in vitro* 3D models at large scale for the market that could lead to a lot of advantages. In our case only a first pilot study has been carried out with a well-stablished cell line to see the impact of the 3D intestinal structure on fibroblasts, but after checking these firsts results further experiments could be carried out and with several cell types and even more relevant in terms of real intestine nature maybe to end up mimicking the whole layers of the intestinal tissue with controlled effects on cells. Because of these first experiments the consequences of the different topographies on the several cell types could be revealed, thus leading for example to the possibility of fully-functional in vitro created organs.

There is still a lot of road ahead, but even though the first application it comes to the mind is creating fully functional artificial organs for human transplants, there are many more useful applications that would make these research works altogether very valuable. If we can find a technique to design exactly the structure of human tissues, like the sinusoidal surfaces in the intestine that have the desired impact and effects in the cells allowing to mimic the natural body response and with a material that is completely biocompatible in order that cells can live, evolve and interact like in our bodies, mimicking tissue characteristics and mechanical properties, these organ models could be used to avoid experimentation with animals, avoiding a lot of ethical concerns and animal suffering, and it could be used in first clinical trials *in vitro*, as it would be almost like inserting any drug that needs to be tested into the patients' body, which would be very useful in everyday work at research laboratories.

Therefore, it would be not only for clinical use like organ transplant but in early stages in experiments and *in vitro* tests, for example for toxicological studies or drug screening, being more reliable rather than for instance just culturing the cells in a plastic flat surface. Also, if we could get enough progress to reach big corporations so they can produce them at large scale, it would be much less expensive, so it could be regularly used and reduce costs (experimentation with animals require larger investments), thus investing this spare budget in other research purposes making them advance faster.

4. REGULATION AND LEGAL ASPECTS

As it has already been explained before, translation from 2D to 3D cell cultures presents many advantages in the research of cellular biology and their physiological and pathological processes due to the better recreation of the natural environment's structure surrounding the cells. To compensate for the 2D culture drawbacks, the pharmaceutical industry is heavily relying on animal models to carry out several trials for drugs and therapies among others, leading to great suffering and loss of animal lives, which arouse many ethical issues and controversy in nowadays society. In fact, serious concerns exist regarding the biological relevance of animals models, since the ability to extrapolate data to human conditions is limited *(35)*. This is why the advances in the generation of 3D environments mimicking the conditions in the human body, both structurally and functionally, is so important. The main examples of this arising technology are organoids and organ-on-a-chip (OoC), and all the knowledge that can be generated with studies like this project will contribute to speed up in the research of this area. The increasing importance of this field of study has led regulatory agencies to fasten the regulatory processes involving this experimental studies, and in fact the U.S. Food and Drug Administration (FDA) has already set up a program to develop the regulation of human tissue chips to replicate the function of the structure of human organs *(36)*.However, in Europe, despite the extensive use of organoids in basic research, the regulatory framework does not define specific guides or rules to such type of entities and, for instance, drug testing using organoids needs to be done according to a very generic *Guideline on the principles of regulatory acceptance of 3Rs (replacement, reduction, refinement) testing approaches* by the European Medicines Agency (EMA). Besides, the clinical use of organoids currently would need to meet the requirements for cell and gene-based therapies following the good manufacturing practices (GMP) as any other pharmaceutical drug *(37).*

4.1. 3D bioprinting regulation

An important factor to take into account when considering the regulatory context involving this kind of projects is 3D bioprinting. Recently, the European Parliament has published a document discussing the legal and ethical aspects of 3D bioprinting for medical and enhancement purposes *(38).*

The complexity and customization of additive bio-manufacturing (bio-AM) artefacts trigger the need for an assessment of the appropriateness of current rules in the domain of pharmaceuticals, tissues and cells, organs, and others. Given the decentralized character of the 3D bioprinting process and the potential rise of consumer-producer biomanufacturing, the main regulatory challenge is in defining and classifying the products associated with 3D bioprinting. Moreover, developments in bio-AM, such as data sharing and customized risk-related products, may eventually bring current medical practices into the domain of the protection of intellectual property rights (IPR) and data ownership under pressure. Another issue that arises is the fact that biological and non-biological materials are regulated in different ways, and both can be used in 3D bioprinting processes.

4.1.1. Legal classification of 3D printing

There is questioning about the exact legal nature and specific categorization of bioprinted materials or bioprinters as machines used for a medical purpose. However, the legal classification of these

products is key considering that different rules applying to biological and non-biological materials can lead to complications for combined products, such as a 3D printed scaffold on which living cells are cultured. Nevertheless, the selection of a particular legal basis like the Advanced Therapies Regulation, may lead to a remarkable regulatory burden regarding market approval requirements. At the same time, the legal classification of 3D printing is extremely difficult due to its custom-made character, and current established pillars of European Union (EU) regulation seems to be unsuitable for bio-AM.

4.1.2. Safety and ethical issues

To ensure the quality and safety of cell and tissue material used in bio-printing, the early stage of donation, procurement, and testing of tissue and cells is governed by the EU Tissues and Cells Directive (EUTCD) 2004/23. Also, the location of manufacture matters in terms when establishing the compatibility of a 3D printing with biological materials and the printing process. It can be carried out in a laboratory with controlled conditions and safety standards or a production plant with quality assurance practices in place, but nowadays a 3D printer can be stored at home by a private owner with very different conditions. Cells and living tissues should be handled under strict safety procedures as in laboratories.

A major ethical concern is that this technology can be misused to improve organs by adding functions or interbreeding human cells with those of animals to give a competitive edge over other individuals. Also, the high cost of the bioprinting manufacturing process and the required production capacity raise social and distributive justice questions of fair and equal access to these products and technology.

Another issue that has to be considered is that the broader 3D printing ecosystem face cybersecurity and privacy challenges, as well as intellectual property (IP). With the use of CAD designs in order to later be printed, the dissemination of the file might be considered an infringement of the IP rights, and the dissemination of the 3D replica may be an infringement of design rights. Also, when using CAD designs coming from medical images of real patients it is faced the risk of loss or stealing of personal data, compromising the privacy of the subject. So, these processes require to be subjected to the privacy protection offered by the General Data Protection Regulation (GDPR).

4.2. Biosafety and ethical issues of the project

Based on the work focus of the project, no major conflicts with ethical principles were expected. Still, all fundamental ethical codes have been respected and performed following the basic ethical principles described in the “Charter of Fundamental Rights” of the European Union (2010/C 83/02). All planned activities and experiments were in conformance with national and EU legislation, regulations, and ethical standards.

Regarding the safety in the laboratory, the work has been performed in accordance with the Directive 2000/54/EC. Personal protective equipment (PPE) has been used including lab coats, gloves and masks among others. Cell culture manipulation has been done on a Class II Biosafety cabinet. Cell culture rooms at Institute for Bioengineering of Catalonia (IBEC) are classified as

biosecurity level P2, suitable for this cell culture processing. Finally, bioprinting procedures were carried out in the 10,000 class clean room of the facilities.

5. CONCEPTION ENGINEERING

The realization of this project consisted of a series of processes that can be summarized in the following objectives, leading to the different tasks and subtasks for the experimental work:

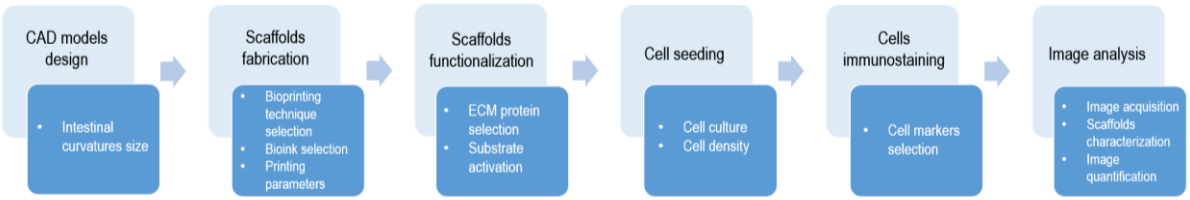

Figure 11: Schematic of the project workflow.

CAD models design: several CAD models mimicking the crypt-villi microstructure of the intestine will be designed to later print them.

- Task 1.1: search in the literature the size range of the intestinal crypts and villi.

Scaffolds fabrication: the previously designed CAD models will be fabricated using 3D printing in order to obtain the scaffolds with different curvatures to later perform the cells experiments.

- Task 2.1: select the most suitable printing technique to fabricate the desired scaffolds.
- Task 2.2: select the most adequate bioink to print the hydrogels.
- Task 2.3: select the optimal printing parameters in order to have as much resolution as possible to fabricate different curvatures.

Scaffolds functionalization: modify the scaffolds' surface to allow a better cell attachment and mimic the ECM.

- Task 3.1: select the ECM protein with which the surface will be functionalized.
- Task 3.2: activate the scaffolds' surface in order to allow the crosslinking of the ECM protein to it and obtain a successful functionalization.
- Task 3.3: assess if the hydrogel functionalization has been successful.

Cell seeding: seed NIH-3T3 fibroblasts in the scaffolds to later be able to see the impact of the different curvatures in the substrate on their behavior.

- Task 4.1: cells will be cultured in order to maintain them throughout the project and have them available to perform the different experiments.
- Task 4.2: determine the optimal number of cells per scaffolds in order to later allow a better analysis of the desired features.

Cells immunostaining: perform different immunostainings of the cells to later be able to acquire confocal images and evaluate the impact of substrate curvature on different cell aspects.

- Task 5.1: select the different markers to analyze the desired characteristic of the cells which might be altered by substrate curvature.

Image analysis: the resulting images obtained through confocal microscopy will be analyzed in order to detect possible changes in different aspects of cell behavior.

- Task 6.1: image acquisition of the scaffolds and the cells with confocal microscopy.

- Task 6.2: characterization of the scaffolds to assess the sizes of the different crypts and villi and determine the different curvatures.
- Task 6.3: the different cell markers are quantified in different curvature regions in order to determine if these changes in curvature trigger changes in cell behavior, density,…

5.1. 3D Printing techniques

To achieve the desired substrate curvatures, one of the 3D printing methodologies reviewed in section 2.5 has to be used to obtain the microstructured scaffold from the hydrogel solution.

5.1.1. Techniques comparison

Extrusion-based printing is the most widely used method at present, being its greatest advantage the capacity for printing a very wide range of biocompatible materials (from 30 to $6x10^7$ mPa/s), in which high-viscosity materials provide structural support whereas low-viscosity materials provide a suitable environment for maintaining cell viability and function. Also, the set-up of this kind of printers is quite simple, even commercial plotters or desktop 3D printers can be easily converted into extrusion-based bioprinters, making them suitable for low-customized services. *(30)* However, it has some disadvantages when compared to the other available methods. The printing accuracy is limited to 100 μm, the bioink needs to meet conditions including gelation, curing and shear thinning properties, and they are difficult to clean.

DOD inkjet printing and LAB are the two mostly used droplet-based bioprinting techniques. Commercial inkjet printers are affordable and easily convertible to bioprinting devices, which makes DOD the lowest-cost technology, and it has also a fast-printing speed. However, the range of suitable biomaterials is narrowed due to the limitations in viscosity. Besides, there are many other issues related to the nozzle that have been commented before. *(30)* Taking all this into account, LAB shows many advantages in front of DOD inkjet printing and extrusion-based methods: the nozzle-related downsides are avoided, and a wider range of materials can be used. Nevertheless, it has also several drawbacks, among them a quite high cost, a lack of availability in commercial printing devices and suitable hydrogel materials, and it is more time-consuming. In some cases, the device contains a metal absorption layer the evaporation of which might cause metal residue to appear in the final structures.

If we look now at photocuring-based techniques, they show a great resolution and are not affected by nozzles nor shear stress. From the two methods, DLP appears to be the best one, and also performs better than extrusion and droplet-based technologies, having a faster printing speed as the printing time per layer does not increase regardless of the structure. *(30)*
In addition, whereas inkjet bioprinting tends to form artificial interfaces between droplets or extrusion-based has to deal with adjacent fibers, DLP technology can fabricate 3D constructs much smoother, leading to high structural integrity and mechanical properties.

	Extrusion-based	Inkjet (Droplet-based)	Photocuring-based
Resolution	100 µm	30 µm	20-50 µm
Fabrication speed	Medium	Fast	Fast
Cell compatible	Yes	Yes	Yes
Support structure required	No	Yes	Yes
Cost	Low	Moderate	Moderate

Table 2: Comparison between printing techniques. Adapted from Ramiah et al. 2020 and Placone et al. 2018. (25,39)

5.1.2. Technique selection

After considering the characteristics of the main different existing bioprinting technologies described in detail in 2.5., the method chosen to print the desired structures for this project is a photocuring-based approach: digital light processing-stereolithography (DLP-SLA). The main reasons to make this choice are the advantages it presents in terms of speed and resolution Looking at the equipments available in IBEC facilities, we had two main options based in a photocuring approach: MJBA Mask Aligner (*SUSS Microtech*) and Solus DLP 3D Printer (*Junction3D*).

The Mask Aligner (Fig. 12) is a UV-photolithography technique widely used in microfluidics, optoelectronics,... and by choosing the appropriate UV-sensitive photoresist a resolution of up to 1 µm can be achieved. This equipment acts in a range of 305-450 nm by means of a 350W Hg lamp as light source. On the other hand, the DLP 3D printer (Fig. 13) uses an HD projector to direct light and create sub-millimetric 3D structures. Furthermore, the projector allows to flash a single image at each material layer, which increases the fabrication speed. The layer thickness, the printing parameter that determines the z resolution, ranges from 10 µm to 100 µm.

Figure 12: MJBA Mask Aligner.

First, it was decided to try the Mask Aligner, mainly because of its great resolution and speed. However, compared to the Solus 3D printer, which was tested later, the results were not as good as expected, especially when controlling the growth of the structures at the desired size. The height of the structures depended on the time that the material was exposed to UV light, which made it difficult to properly adjust the exposure time to achieve the desired structures, and unlike the Solus 3D printer, the starting point was not a CAD design but rather an acetate photomask, thus complicating the in-demand tunning of the design. The results obtained with this equipment are detailed in section 6.1, and the method used for printing is detailed in section 5.4.5.

After a first test with the Mask Aligner, the other choice that was tried was the Solus 3D Printer. The resolution of the solution that was intended to be used had to be determined in situ, but once it was tested and the firsts results were obtained, the final decision was to carry on with the experiments using this printer. The resolution obtained using the chosen bioink allowed working within the range that comprises the anatomical size of the small intestine architecture of crypts and villi, so the Solus seemed to be a good option to work with. The 3D printer solus was initially designed to print hard resins, and consisted of the following main components: a facing-down printing support coupled to a Z-axis motor, a resin vat with a transparent window, and a beam projector. The system was customized by members of the lab by including an aluminum printing support 12 mm of diameter that enabled the printing of small samples (between 3 to 10 mm in diameter) and an aluminum vat of 20 mm of inner diameter allowing the use of reduced prepolymer volumes (down to 2 mL). Aluminum was chosen for its good thermal conductivity and its lower oxygen permeability, whereas a FEP film of 150 µm in thickness was used to create a flexible transparent window at the bottom of the vat to allow the patter transfer to the solution and at the same time creates an oxygen permeable window to tune the free radical photopolymerization reaction. In addition, a flexible heater with a thermostat was coupled to the system to keep the prepolymer solutions at 37ºC preventing physical gelation. Finally, a full High-Definition 1080p resolution projector (*Vivitek*) was employed to crosslink the polymeric network using visible light by reflecting it in the mirror under the printer and from there illuminate the solution.

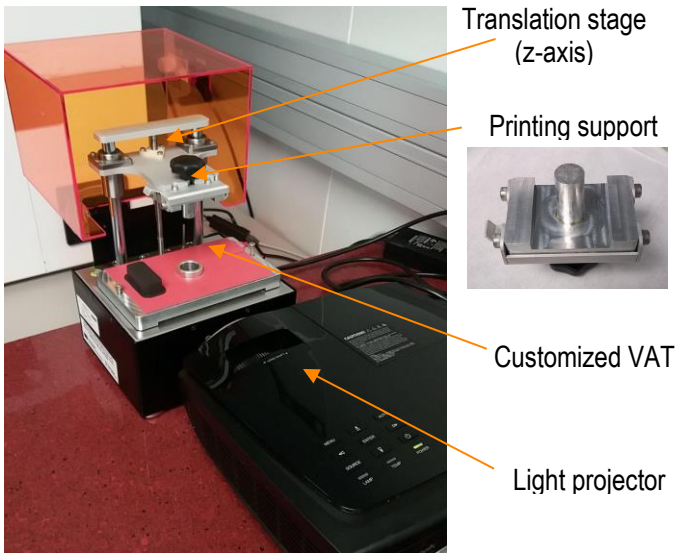

Figure 13: Modified Solus 3D Printer

5.2. Hydrogels comparison and selection

Photocrosslinkable hydrogels, including the above-mentioned PEGDA, GelMA and methacrylated hyaluronic acid (MeHA), have been extensively explored in biomedical fields, especially for 3D tissue engineered constructs, such as the hydrogel scaffolds that have to be fabricated in this project. This is due to their great properties like good biocompatibility, hydrophilicity and biodegradability. Because of the many advantages mentioned above and being the light considered an ideal external control to tune the hydrogel's properties, for this project it has been decided to use photocrosslinkable hydrogels.

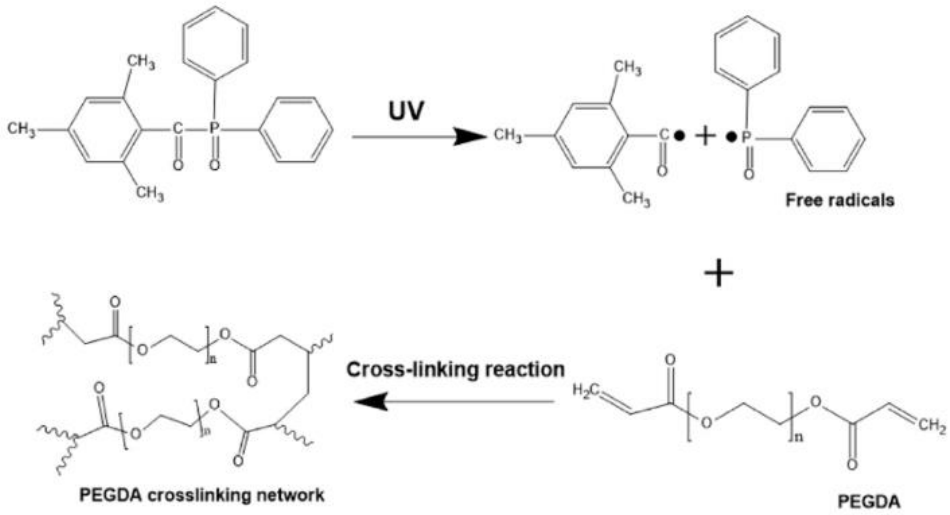

Figure 14: Photocrosslinking process of PEGDA. Adapted from Yang et al. 2015. (40)

Briefly, the general process to synthesize the three hydrogels (Fig. 14) is as follows: in the presence of a light source, the photons absorbed by the photoinitiators promote their cleavage, leading to a formation of free radical molecules. These reactive molecules react with the vinyl bonds in the pre-polymer, leading to the formation of chemical crosslinks between polymer chains *(27)*.

After considering the several pros and cons of the three options, for this project the choice has been PEGDA, one of the derivatives of PEG. From it, PEGDA is fabricated by substituting terminal hydroxyl groups of PEG with acrylates. It is a non-degradable synthetic polymer that forms mechanically stable networks *(41)*. Its double-bond acrylate groups at each end of the PEG chain allow it to undergo free radical initiated chain photopolymerization in the presence of a photoinitator to form a 3D polymer network. While it can be crosslinked by various methods, the use of photopolymerization is especially versatile for use in biomedical applications.
PEGDA hydrogels can be fabricated fast and easily, and their mechanical properties can be simply tuned by varying the concentration or molecular weight of the polymer *(27)*. So, compared to GelMA and MeHA, it is more easily synthesized and tuned, and the mechanical properties can be easily modified, thus making it suitable for a wide range of applications, including the generation of hydrogel scaffolds, and therefore making it an appropriate choice for this project combined in a prepolymer solution with other components that will be detailed in section 5.4.3.

5.3. Materials

All the reagents and materials used throughout the project are detailed in the list below in alphabetical order:

- Acetic acid – Panreac
- Acrylic acid – Sigma-Aldrich
- Albumin from bovine serum – Thermo Fisher
- Alexa Fluor® 488 anti-mouse – Life Technologies
- Alexa Fluor® 568 phalloidin – Life Technologies
- Alexa Fluor® 647 anti-rabbit – Life Technologies
- Bovine Serum Albumin – Sigma-Aldrich
- BupH™ MES Buffered Saline Packs – Life Technologies
- Collagen Type I solution from rat tail – Sigma-Aldrich
- DAPI (4',6-diamidino-2-phenylindole) – Life Technologies
- Dow Corning® High-Vacuum Grease – Sigma-Aldrich
- Dulbecco's Modified Eagle Medium (DMEM), high glucose, no glutamine – Life Technologies
- EDC (1-Ethyl-3-(3-dimethylaminopropyl)carbodiimide)
- Ethanol absolute – Sigma-Aldrich
- Fetal Bovine Serum – Gibco
- FluoromountTM Aqueous Mounting Medium – Sigma-Aldrich
- Formalin solution, neutral buffered, 10% – Sigma-Aldrich
- Hanks' Balanced Salt Solution – Sigma-Aldrich
- Irgacure 2959 – Sigma-Aldrich
- Lithium Phenyl(2,4,6-trimethylbenzoyl)phosphinate – TCI
- Milli-Q water – Sigma-Aldrich
- Mouse Anti-Vimentin cell signaling antibody – Abcam
- Mouse Anti-YAP antibody – Santa Cruz Biotech
- NHS (N-Hydroxysuccinimide) - Sigma-Aldrich
- Normal Donkey Serum – Abcam
- Normocin™ - InvivoGen
- Penicillin-Streptomycin – Gibco
- Phosphate Buffered Saline solution 10X – Fisher Scientific
- Poly(ethylene glycol) diacrylate average Mn 6,000 – Sigma Aldrich
- Rabbit Anti-Fibronectin antibody – Sigma-Aldrich
- Rabbit Anti-Laminin antibody – Abcam
- Rabbit Anti-Paxillin antibody [Y113] – Abcam
- Silane 3-(Trimethoxysilyl) propyl methacrylate – Sigma-Aldrich
- Tartrazine Dye content ≥85 % – Sigma-Aldrich
- Triton™ X-100 – Sigma-Aldrich
- Trypsin-EDTA solution 10x – Sigma Aldrich

5.4. Methods

5.4.1. Cell line culture

NIH-3T3 fibroblasts (ATCC® CRL-1658™) were cultured in Dulbecco's Modified Eagle Medium (DMEM) supplemented with 10% Fetal Bovine Serum (FBS) and 1% Penicillin-Streptomycin (P/S) and maintained at 37ºC in a humidified incubator under a 5% CO_2 atmosphere.
Cells were passaged twice a week, with a split ratio of 1:10 using 25 cm^2 culture flasks. Briefly, first the cell media was removed and cells were carefully rinsed with Phosphate Buffered Saline solution (PBS). Then, PBS was aspirated and Trypsin-EDTA was added and incubated for 5 minutes at 37º in order to detach the cells. Next, Trypsin-EDTA was neutralized by adding culture medium to the flask. Then, the whole volume of this medium along with the trypsinized cells was centrifuged at 1200 rpm for 5 minutes. Once centrifuged, the supernatant was removed, and the pellet containing the cells was resuspended using 1 mL of new culture medium. Finally, the selected volume of medium with cells according to the 1:10 ratio was transferred to a new flask with 7 mL of culture medium and maintained in the incubator.

5.4.2. Coverslips silanization

In order to be able to use glass coverslips as a printing substrate for our designs, they had to be activated by means of the silanization procedure described here, which allowed the formation of a covalent bound between the hydrogel and the glass coverslip. First, coverslips were placed in a glass Petri dish avoiding overlapping between them and they were exposed to an ozone plasma treatment for 15 minutes. After the exposition, 5 mL of silanization solution were added per Petri dish. This solution was prepared with 5 mL of absolute ethanol, 100 µL of Silane 3-(Trimethoxysilyl) propyl methacrylate (2%) and 150 µL of an acetic acid solution with Milli-Q water (1:10). The coverslips were incubated with the silane solution for 2 hours in shaking conditions. Then, the solution was removed and 96% ethanol was added covering the coverslips and removed thrice, the last time incubating the dish 5 minutes in the shaker before removing the ethanol. Finally, the Petri dish containing the coverslips was placed in the oven at 65ºC for 1 hour and kept in the desiccator until use.

5.4.3. Prepolymer solutions preparation

The prepolymer solution used to print the villi-like scaffolds with the Solus 3D Printer on glass coverslips by photopolymerization was prepared in a glass vial with 6.5% w/v of PEGDA with a molecular weight of 6000 Da ($PEGDA_{6000}$), 0.4% w/v of visible-light lithium phenyl-2,4,6-trimethylbenzoylphosphinate (LAP) photoinitiator, 1% w/v of AA and 0.025% w/v of tartrazine food dye. This last component was added to minimize the undesired overexposure effect and have a finer control of the photocrosslinking process because of its photoabsorber role. All the components were dissolved in Hank's Balanced Salt Solution (HBSS) supplemented with 1% of P/S and 1:500 of Normocine. Once all the components were added, the solution was dissolved by placing the vial on a hotplate at 65ºC, and finally kept in the fridge at 4ºC until use.

Regarding the Mask Aligner solution, 6.5% w/v $PEGDA_{6000}$, 1% w/v Irgacure D-2959 photoinitiator and 0.3% w/v AA were dissolved in filtered PBS 1x at 65ºC, and then stored in the fridge until use.

5.4.4. Design of CAD models

As mentioned before, the printing process of the definitive hydrogel scaffolds was performed in a customized Solus 3D Printer, which works with a DLP projector that reaches an XY resolution of up to 25 µm and a layer thickness up to 10 µm, and it is based on the DLP-SLA technique. This printer is connected to a computer allowing to select the desired printing parameters and the designs previously created with CAD tools in order to fabricate the models with the desired features. So first of all, the desired microstructures had to be designed with the proper characteristics in order to be later transferred to the printer software and be fabricated. The designs to be printed were created with CAD tools using the *FreeCAD* software, and then they were exported to *.stl* format to be able to do the slicing of the design and print it layer by layer. The structures were designed in the shape of 6 mm discs as a base and with the crypt-villi architecture typical of the small intestinal tissue.

5.4.5. Hydrogels printing procedure

After all the materials and the desired designs were ready, it was possible to start the fabrication of the hydrogels with the 3D printer. Once in the clean room, the prepolymer solution was filtered and poured into the adapted vat of the printer. Then, by means of a circular double-sided pressure sensitive adhesive (PSA) piece, a 12 mm diameter glass coverslip was attached to the printing support, which was next coupled to the printer. After, the layer-by-layer printing of the hydrogel was initialized, consisting in the repetition of 3 steps: submerging the printing support in the solution, the projector illuminating the solution for a given time, and the rising of the printing support to the initial position. The software of the printer allowed also to modify the parameters that affect the final result and resolution, so all the structures with different sizes are fabricated, and adjust the adequate values for each situation. In this case, layer thickness was set to 13 µm, layer exposure time to 10 seconds and initial layer exposure (in this case the first two layers) to 25 seconds. In addition, the printer can work with two resolutions, from which it was chosen the high resolution of 48x27.
Once the printing process was finished, the entire sample (coverslip and hydrogel) was detached from the support and rinsed with PBS to remove unreacted polymer. Finally, it was transferred to a cell culture well plate and stored in PBS 1x at 4ºC until further use.

The printing of the hydrogels with the Mask Aligner was performed following the next steps. (Fig. 15) First, a set of PDMS (10:1 w/w prepolymer with the curing agent) pools was placed on the base of the outer surface of a Petri dish, avoiding bubbles and ensuring a proper attachment pressing with tweezers. These pools had been previously punched and two inlet channels connecting them had been carved in order to later be able to introduce the hydrogel prepolymer solution. They had a diameter of 6 mm and a height of 0.5 mm. Then, silanized glass coverslips were placed centered on top of each PDMS pool and attached by gentle pressing. Once all this set up was prepared, the prepolymer solution was pipetted into the pools gently to avoid the formation of bubbles by putting

the pipette at the beginning of the channels in the intersection between the coverslip and the PDMS pool. After filling all the pools, the base of the inner surface of the Petri dish was covered with a black paper in order to avoid the scattering of light because of the transparent substrate of the Petri dish and make it impact vertically when irradiating with the UV light, and on top of the coverslips a patterned photomask was placed in order to fabricate the desired microstructures by means of classic lithography. The photomask had been previously designed and fabricated by members of the lab. Briefly, it was designed using *AutoCAD* software (*Autodesk*) and printed on acetate films, which consisted of dark circles of 300 µm of diameter and were separated 500 µm from center to center. To photocrosslink the prepolymer solution, the pools were exposed to UV light in the Mask Aligner for 50 or 60 seconds using the Flood Exposure mode. After UV exposure, unreacted polymer was washed out by rinsing with filtered PBS 1x and the coverslips with the attached hydrogels were separated from the pools and placed in a well plate with PBS 1x after removing the part that had polymerized in the channels region and did not correspond to the desired microstructure. Finally, the samples were stored at 4ºC until further use.

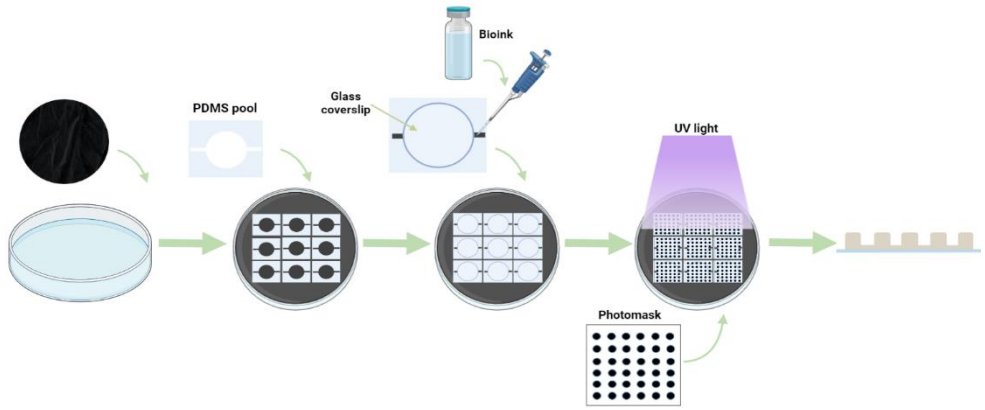

Figure 15: Fabrication procedure for the Mask Aligner.

5.4.6. Hydrogels functionalization

In order to later be able to seed the cells and evaluate the several aspects mentioned before, the hydrogel scaffolds had to be functionalized. The selected protein to functionalize the hydrogels was collagen, the most abundant protein within the ECM, representing up to 30% of the total protein mass of a multicellular animal. In addition, it provides tensile strength, regulates cell adhesion and supports migration among other functions, therefore allowing the ECM to provide essential physical scaffolding for the cells *(42)*. The chosen method used EDC and NHS reagents. First of all, the hydrogels in the wells were submerged in MES buffer (0.1 M, pH 4.7) and each component was weighted in a different vial. Then, NHS was dissolved in MES buffer at a concentration of 100 mM, which in turn was diluted 1:2 when EDC was incorporated, achieving the desired concentration of 50 mM. The resulting solution was then sterilized by filtration through a 0.22 µm filter. Afterwards, the MES buffer was removed from the wells and the EDC was dissolved in MES buffer, which was also diluted 1:2 when added to the same tube of the NHS reaching the 25 mM concentration. This solution was also filtered through 0.22 µm and incorporated in a tube together with the NHS solution, having the same volume of both solutions. Then, the hydrogels in the wells were covered with the necessary volume of the final solution and they were left to incubate 30 minutes shaking

at 100 rpm at room temperature (RT). After the incubation, hydrogels were rinsed twice with sterile PBS 1x and the second time they were left to incubate 5 minutes in shaking conditions at RT. Then, a protein solution consisting of collagen type I dissolved 1:10 in PBS 1x was added to each well and the hydrogels were left to incubate overnight at 4ºC in shaking conditions. Finally, each well was washed twice with PBS 1x.

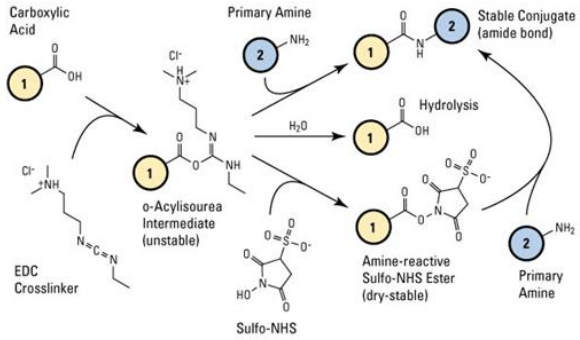

Figure 16: NHS-EDC reaction to functionalize scaffolds.

5.4.7. Cell seeding

To see the effect of the curvature on cells, these were seeded on the functionalized hydrogels. (Fig. 17) In order to achieve an appropriate placing of the cells, first the hydrogels were placed in a new dry well plate in a centered position within the well, and afterwards a PDMS ring that fitted the well dimensions and had enough inner diameter in order to host the hydrogel in the middle was placed and attached using Dow Corning-High vacuum grease. Then, PBS was added to prevent the hydrogels from drying.

Once all the wells were set up with the corresponding rings, a cell passage explained in 5.3.1 was performed until the resuspension of the pellet step. There, the resulting volume was diluted adding cell culture medium up to 10mL and from there cells were counted using a Neubauer's chamber. Once obtained the total number of cells in the whole volume, the desired cell concentration was prepared in a tube with 200µL of medium, and then trespassed to the well, therefore seeding the cells over the hydrogel scaffold, after having removed the PBS. Several cell densities ranging between 1,000 and 20,000 cells per scaffold were tested in order to find the optimal for the experiments, and finally it was determined that the best one in this case was 10,000 cells.

Finally, after letting the cells attach to the substrate for 1 hour, 1.25 mL of medium per well were added.

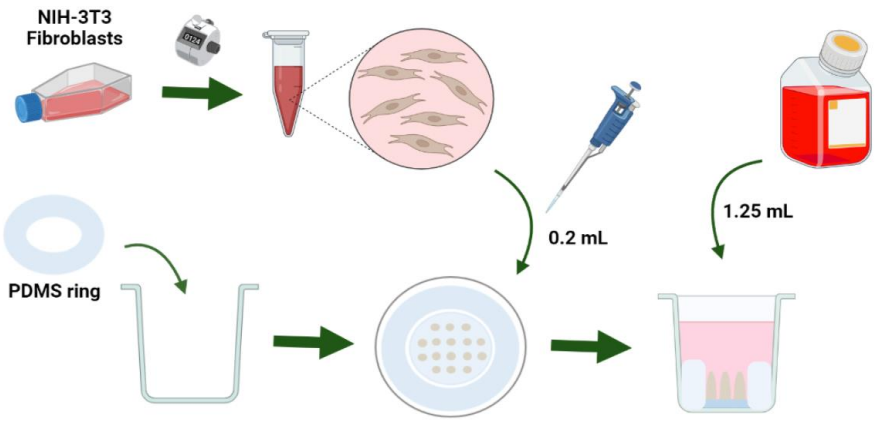

Figure 17: Cell seeding procedure.

5.4.8. Hydrogels immunostaining without cells

In order to characterize the scaffolds in the confocal microscope, an immunostaining of the hydrogels was performed. First of all, filtered blocking buffer (10% BSA (bovine serum albumin) 10%, 3% donkey serum in PBS 1x) was added to each well and incubated for 30 minutes shaking at RT. Then, blocking buffer was removed and primary antibody was added diluted in filtered Ab buffer (0.1% BSA 10%, 0.3% Donkey Serum in PBS 1x) to each well and incubated for 1 hour shaking at RT. Afterwards, the primary antibody solution was removed and each well was washed 3x with PBS 1x. Then, the secondary antibody was diluted in filtered Ab buffer and added to each well incubating for 45 minutes shaking at RT avoiding light exposure from this step on. Finally, each well was washed 3x with PBS 1x and either stored at 4º or directly mounted using Fluoromount-G or PBS to inspect them under the confocal microscope.

5.4.9. Immunostaining with cells

In this case, the immunostaining procedure is for hydrogel samples with seeded cells on them, so after cell seeding this process would be carried out instead of 4.3.7. First of all, the samples had to be fixed in order to stop cell growth. To do so, first the media was removed and each well was washed 3x with warm filtered PBS 1x. Then, PBS was removed and formalin was added and left incubating for 30 minutes shaking at RT. Afterwards, the formalin was removed and samples were washed 3x with PBS 1x. To continue, PBS was removed and permeabilization buffer (0.5% Triton X-100 in PBS 1x) was added and incubated for 30 minutes shaking at RT. Then, this buffer was removed and samples were washed once with PBS 1x. After permeabilization, blocking buffer (10% BSA 10%, 3% donkey serum, 0.2% Triton X-100 in PBS 1x) was added and left to incubate for 2 hours shaking at RT. Then, it was removed and primary antibodies were added diluted in primary Ab buffer (0.1% BSA 10%, 0.3% donkey serum, 0.2% Triton X-100 in PBS 1x) leaving the sample to incubate overnight shaking at 4º wrapped in parafilm. The following day, the primary antibodies solution was removed and samples were washed 5x with PBS 1x at RT. Then, secondary antibodies, F-actin and DAPI diluted in secondary Ab buffer (0.1% BSA 10%, 0.3% Donkey Serum in PBS 1x) were added and left incubating for 2 hours shaking at RT, avoiding light exposure from this step on. Finally, the secondary antibodies solution was removed, samples were washed 5x with PBS and they were either stored at 4ºC or directly mounted using PBS to inspect them under the confocal microscope.

5.4.10. Image acquisition and analysis

Once the samples were immunostained, images were acquired with a LSM 800 confocal laser scanning microscope (*ZEISS*) with 5x (NA = 0.16) and 10x (NA = 0.3) air objectives and analyzed using ImageJ software. The pinhole diameter was set to 1 Airy Unit (AU), and for the z-stacks the z-step was set to 7.5 µm.

5.4.10.1. Curvature assessment

After acquiring the confocal images of the different crypts and villi, it was necessary to assess the resulting curvature of each kind of structure within the hydrogels and compare them to the

theoretical values from the CAD models we had designed with the desired features. To do so, in the case of the theoretical designs it was calculated the inverse of the radius of the cylinders or spheres that were necessary to build the villi and crypts models and from here the curvature value was obtained. A schematic of the theoretical design can be seen in Fig. 18 a). Regarding the fabricated scaffolds, because the shape was more cone-like rather than cylindrical, there were different curvatures along the height of both the villi and the crypts, so it was necessary to measure the curvature at different slices of the hydrogels. In the case of the villi, as it can be seen in Fig. 18 b), a circle was fitted at the base, another at the middle and another at the top region. These were the curvatures seen from the top view, but there was also a curvature at the top seen from the orthogonal cross section. So, all in all, using the autofluorescence of the hydrogel acquired using the confocal microscope, first the total number of slices that composed the villi image was determined, then it was divided into two equal regions (therefore obtaining three cuts where to measure the curvature: beginning, middle and end) and in each significant slice (top, middle and base) a circle was fitted. Then, the area of the circles was calculated, and using the formula $A = \pi r^2$ the radius was isolated and calculated, in order to finally calculate its inverse and obtain the curvature value.

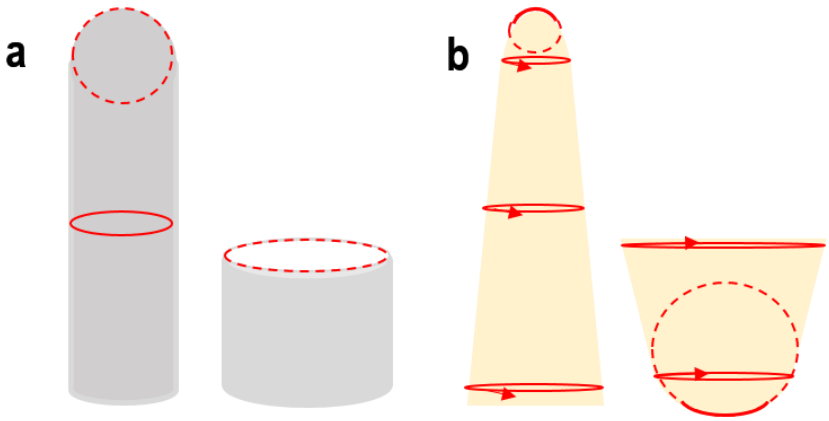

Figure 18: a) Schematic of the regions of the theoretical villi and crypt from which to measure the curvature. b) Schematic of the regions of the fabricated villi and crypt from which to measure the curvature.

Regarding the crypts, the process was quite similar as it can be seen in Fig. 18. The calculus was performed in the same way, but in this case, because the crypts were much lower than the villi, only two top view curvatures were determined, the top and the bottom, and then also the cross section of the bottom.

In both cases, the curvature was determined for each sample we had fabricated for the several experiments, and from here the mean was calculated for each region and kind of sample.

5.4.10.2. Markers' quantification

Apart from acquiring the microstructures images, the cells in the scaffolds were also imaged in order to analyze the different markers. The expression of these markers was measured by quantifying the mean gray value in a region of interest (ROI) in the cell using ImageJ. Briefly, once

the image was open in the software it was performed a *Sum slices* z-project and the desired channel containing the expression of the marker was selected. Then, a circular ROI of constant area through the several images was drawn inside the cells at different curvatures and the mean gray value of this area was measured, thus obtaining the level of expression of the particular marker. In order to make the measurement more reliable, different ROIs were drawn at different regions of the cell, and then the more representative of the mean was selected. Additionally, in the case of YAP, one ROI was drawn inside the nucleus and another in the cytosol, and then the ratio nucleus/cytosol was calculated.

5.4.10.3. Statistical analysis

Data analyses were performed with Prism (*GraphPad).* Statistical differences were analyzed by ordinary one-way ANOVA test. A p-value smaller than 0.05 was considered as statistically significant: (*) $p < 0.05$, (**) $p < 0.01$ and (***) $p < 0.001$.

Regarding cell experiments, 3 experiments were performed for YAP, 2 for laminin, 2 for α-SMA, 1 for vimentin and 1 for fibronectin.

6. DETAILED ENGINEERING

In this section the results obtained are presented and discussed. They have been organized according to the stages that have progressively been completed to achieve the completion of the project: from the development of the CAD models to the fabrication of the different designs of villi and crypts and from these the optimization of the printing parameters and model sizes to obtain the best microstructures possible, and finally the results obtained from the cells' experiments resulting from the samples imaging and posterior analysis and quantification.

6.1. Techniques comparison

As commented above, in order to determine which technique would be the one used throughout the project, first the Mask Aligner was tested. To pattern the hydrogel in the desired design, an acetate photomask consisting of a set of circular black windows of 300 µm of diameter spaced 500 µm from center to center was used. Two batches of samples were performed: one was exposed to UV light for 50 seconds, and another one for 60 seconds. The hydrogel scaffolds with the resulting crypts can be seen in Fig. 19. It can be seen that although from the top view the two different samples have almost an identical appearance, when looking at the cross section the hydrogel that was exposed for 60 seconds has more funnel-shape crypts, whereas the crypts in the hydrogel exposed for 50 seconds are like straight cylinders.

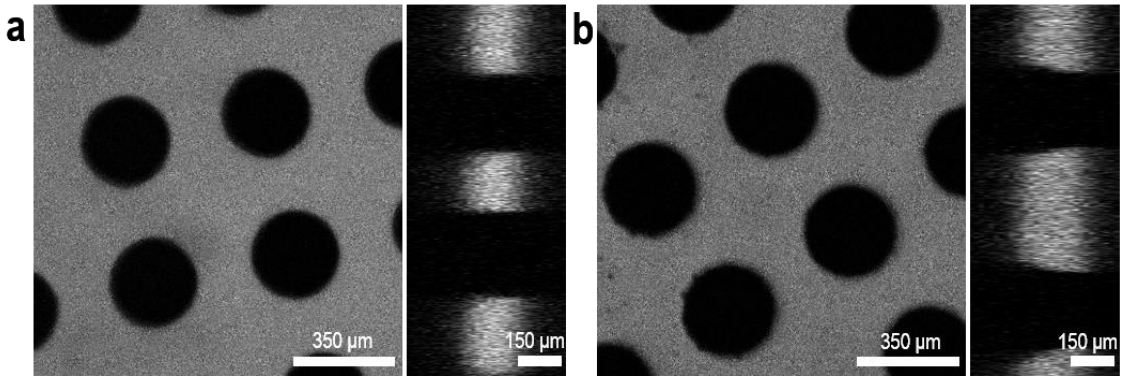

Figure 19: a) Top and cross section confocal images of the 50 seconds crypts scaffolds obtained with the Mask Aligner. b) Top and cross section confocal images of the 60 seconds crypts scaffolds obtained with the Mask Aligner.

Because the growth of the structures depended on the time that the material was exposed to UV, it was complex to control the process and achieve the desired feature. In addition, to produce different patterns, it would have been necessary to design and fabricate new acetate masks containing the desired characteristics, thus rendering it a very slow and expensive process. Therefore, it was decided to perform a test with the Solus 3D Printer, which uses a CAD model as a starting point to fabricate the hydrogels, therefore facilitating the design of new models.

However, the resolution of the bioink (detailed in section 5.4.3) that was intended to use for this equipment had to be determined *in situ* in order to check if it allowed fabricating all the desired microstructures. To do so, it was performed a test consisting of the fabrication of two scaffolds containing both villi and crypts with the characteristics specified in Table 3.

		Height / Depth	Diameter
Scaffold 1	Crypts	150 µm	350 µm
	Villi	1 mm	300 µm
Scaffold 2	Crypts	100 µm	250 µm
	Villi	700 µm	250 µm

Table 3: Microstructures features of the scaffolds fabricated with the Solus 3D printer.

The printing parameters to fabricate the models were a layer thickness of 13 µm, 10 seconds of layer exposure time and an initial layer exposure (for the first two layers) of 25 seconds.

The resulting scaffolds and the CAD models used can be seen in Fig. 20, and it can be observed how in the two different cases both the crypts and the villi were successfully fabricated. So, after considering the pros and cons of both techniques, it was decided to carry out the experiments with the Solus 3D printer.

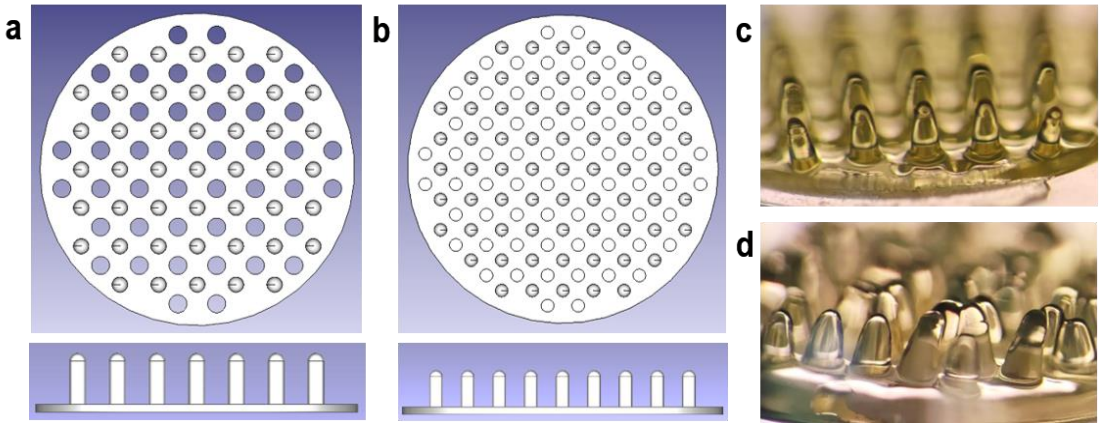

Figure 20: CAD model of 300 µm diameter and 1 mm height villi, and 350 µm diameter and 150 µm depth crypts. b) CAD model of 250 µm diameter and 700 µm height villi, and 250 µm diameter and 100 µm depth crypts. c) Stereomicroscope image of the scaffold corresponding to the CAD model in a). d) Stereomicroscope image of the scaffold corresponding to the CAD model in b).

6.2. CAD models

As it has been said, in order to fabricate the scaffolds with the different microstructures it was first necessary to design the distinct CAD models with the desired features. The base of the scaffolds was the same in all the cases, consisting of a circular support of 6 mm diameter. Then, the design procedure changed whether the microstructures were crypts or villi. In the case of the crypts, they were modeled as straight cylinders with the desired diameters, and then these cylinders were subtracted from the original base disk in order to remove that amount of volume and obtain holes with the diameter of the desired crypts. The depth was adjusted by simply changing the thickness of the base disk. Some of the more representative crypts CAD models can be seen in Fig. 21.

Regarding the villi, the procedure was the opposite. Instead of subtracting the created shapes, they were added to the disk. Basically, cylinders with the desired diameter were created, and in order to achieve the roundish shape at the top to have some curvature, half a sphere was added to the top

of the cylinder with the same diameter as this. Some of the most representative villi models can be seen in Figure 22.

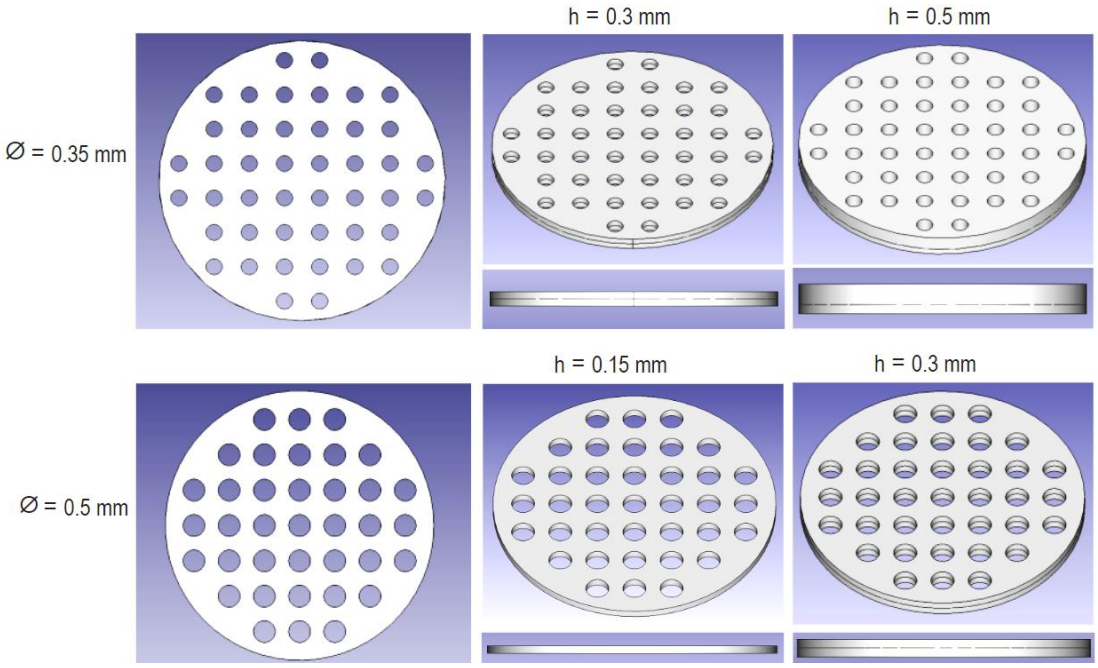

Figure 21: Different CAD models of crypts changing their diameter and depth.

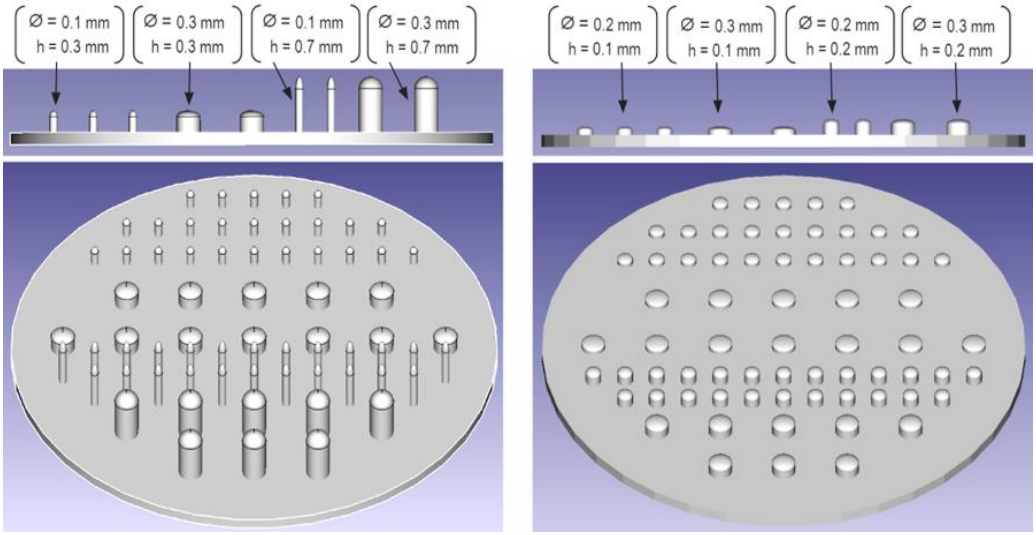

Figure 22: Different CAD models of villi changing their diameter and height.

6.3. Fabricated scaffolds

6.3.1. Crypts scaffolds

Once the different CAD models had been designed, they could be trespassed to the printer in order to fabricate the substrates with different curvatures. Several diameters and depths were tested, obtaining different sets of curvatures. The crypts were designed as a hole throughout the disk, however, due to the resolution limits and light overexposure, the resulting features had a hydrogel

layer at the base, thus successfully obtaining curved invaginations/crypts rather than straight holes. An example of the resulting crypts scaffolds can be seen in Fig. 23.

Nevertheless, due to resolution limitations some of the crypts could not be printed, resulting just in a flat scaffold. The theoretical measures that yielded the most successful crypts are summarized in Table 4.

Depth	Diameter
150 µm	500 µm
150 µm	350 µm
300 µm	350 µm
500 µm	350 µm

Table 4: Summary of the sizes of the most successful fabricated crypts.

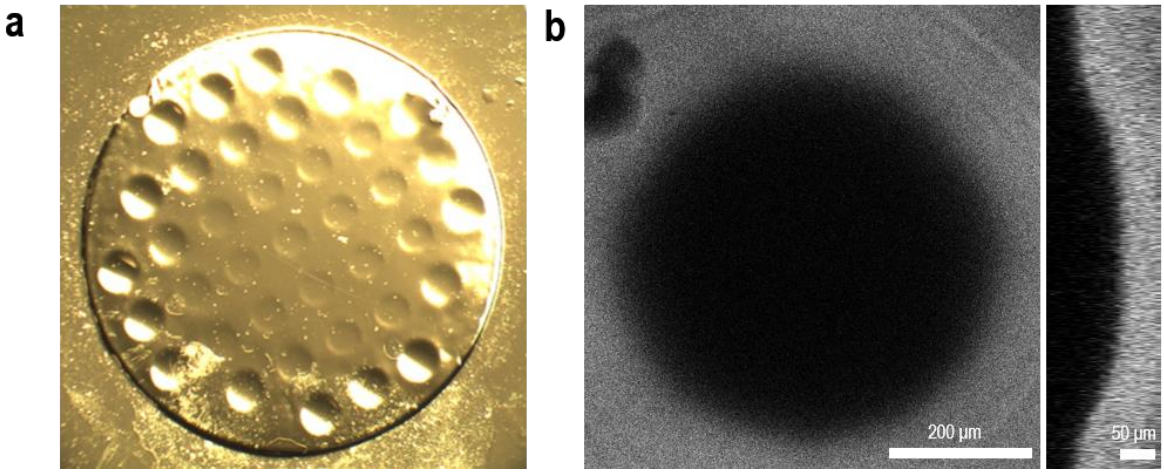

Figure 23: a) Stereo microscope image of 150 µm depth and 500 µm diameter crypts. b) Confocal image 10x of a crypt from the scaffold in a).

6.3.2. Villi scaffolds

Regarding the scaffolds containing villi, the fabricated models consisted of different villi changing their height and diameter. Several models were tested and almost all of them worked well, thus allowing to obtain different ranges of curvature. Some of the most relevant, which later were used for the cells experiments, can be seen in Fig. 24. However, in this case some resolution limitations were also encountered. There were no problems when increasing the sizes of the villi, but when it was tried to thin or shorten them, they were not fabricated as expected from the model. For instance, some of the first villi fabricated had a height of 700 µm and 300 µm, but to optimize their imaging and also obtain a different curvature, some of them were shortened to 100 µm, and in another model they were designed with a diameter of 100 µm. But reducing the sizes to such a scale did not allow the villi to be printed, thus setting the limit for both cases around 200 µm, which still is a good resolution and allowed having different curvature ranges. The theoretical measures of the most relevant fabricated villi are summarized in Table 5. Also, it has to be said that originally in the design the villi were modeled as straight cylinders and half a sphere at the top, when

fabricated the appearance was more of cone-shape, increasing the diameter from the top to the bottom, and thus having different curvatures at different heights.

Height	Diameter
700 µm	300 µm
300 µm	300 µm
200 µm	300 µm
200 µm	200 µm

Table 5: Summary of the sizes of the most relevant fabricated villi.

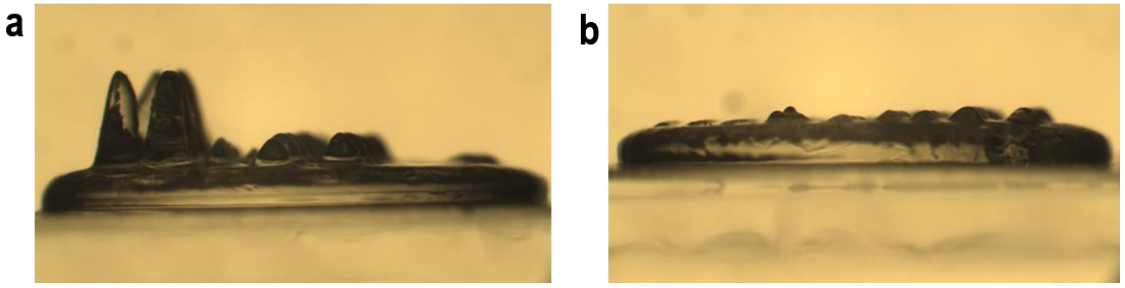

Figure 24: a) Stereomicroscope lateral image of 100 µm and 300 µm diameter and 300 µm and 700 µm height villi b) Stereomicroscope lateral image of 200 µm and 300 µm diameter and 100 µm and 200 height villi.

6.3.3. Optimization of printing parameters

Until this moment, the printing parameters used throughout had not been changed and were the ones specified in 6.1. However, in order to try to fabricate the structures that were not printed with these parameters, it was tried to optimize their values. By adjusting the layers exposure time and the layer thickness, it was intended to increase the resolution of the technique and improve the resulting structures. However, it was encountered that the lower limit available in the printer settings was very close to the one that had been used up to the moment, being of 10 µm and thus not allowing a wide working range to modify the parameter. Nonetheless, several combinations with different values for the three parameters were tested, which are summarized in Table 6.

Layer thickness	Layer exposure time	Initial layer exposure
10 µm	10 seconds	25 seconds
10 µm	5 seconds	25 seconds
13 µm	5 seconds	25 seconds
12 µm	8 seconds	25 seconds
20 µm	10 seconds	25 seconds

Table 6: Summary of the combination of the changes in the different parameters.

Surprisingly, the only one that seemed to work at least equal to the original combination was the one increasing the layer thickness and maintaining the exposure times in the case of the crypts. The others, probably due to the reduction of the layer exposure time, were not correctly fabricated, leaving much prepolymer solution that had not been crosslinked on top of the scaffold, thus not allowing the increase in definition of the structures. Regarding the thinnest villi, probably the issue is in x-y resolution, because the structures start growing but even though the designs were of

different heights, they stopped at the same point thus not achieving the desired height. Some of the resulting scaffolds can be seen in Fig. 25.

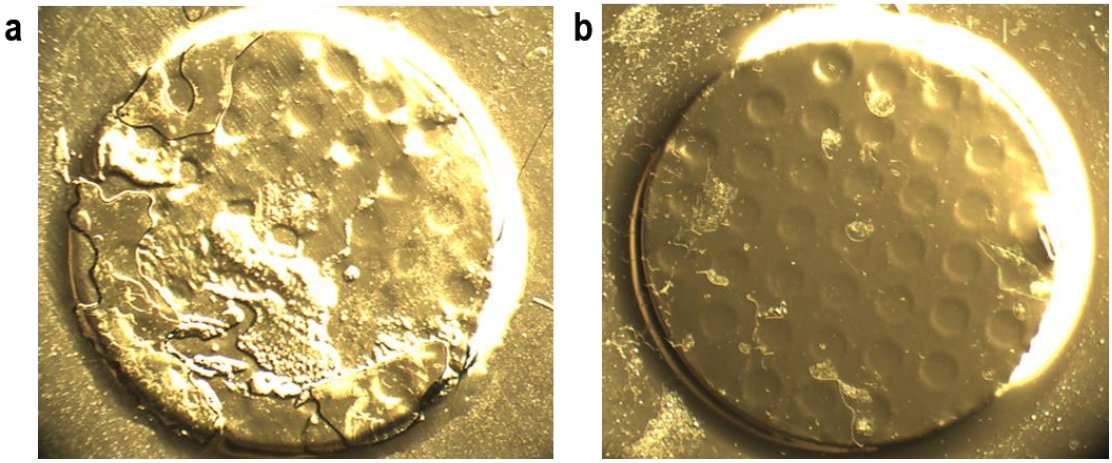

Figure 25: a) Crypts scaffold obtained with a layer thickness of 10 µm and a layer exposure time of 5 seconds. There is much unpolymerized hydrogel on top of the scaffold and the crypts are not well defined. b) Cryps scaffold obtained with a layer thickness of 20 µm and a layer exposure time of 10 seconds. In this case the hydrogel is completely polymerized, but it does not increase the resolution it was already obtained for the crypts scaffold in Fig. ----.

6.4. Scaffolds functionalization

After obtaining the different scaffolds, the next step was to functionalize them, that is, activate and cover the substrate with an ECM protein, in this case collagen type I, that allowed mimicking the natural environment where cells are usually residing. The functionalization process is detailed in section 5.4.6, but it briefly consisted in activating the substrate with NHS and EDC in order to permit the crosslinking of the protein to the scaffold, and then the hydrogels were incubated in a collagen solution. In the case of the villi, the functionalization worked well for all of them, covering all the surface of the structure as it can be seen in Fig. 26, and thus rendering viable all the surface for cells to attach.

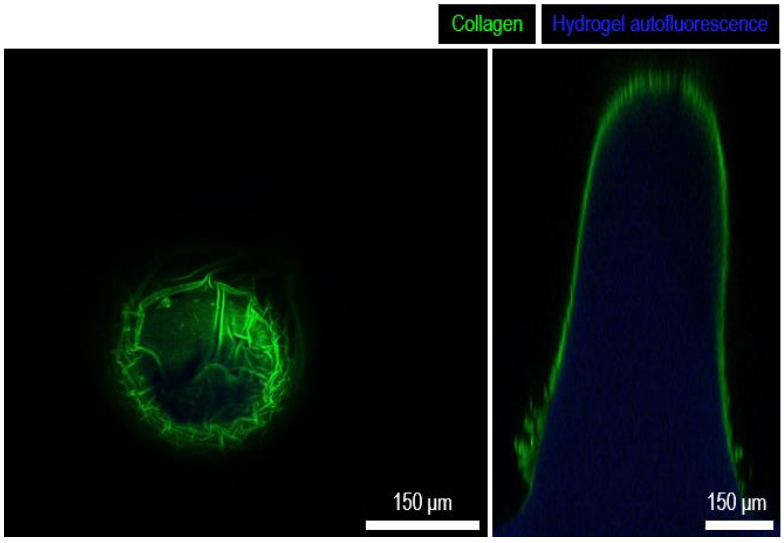

Figure 26: Top (left) and cross-section (right) confocal images of a functionalized villus.

However, in the crypts scaffolds some issues arose. Beginning with the crypts fabricated through the Mask Aligner, it was found out that after the incubation the collagen did not arrive to the bottom of the structure, thus reducing the available substrate for the cells and changing the orthogonal curvature of the crypts. This can be clearly seen in Fig. 27.

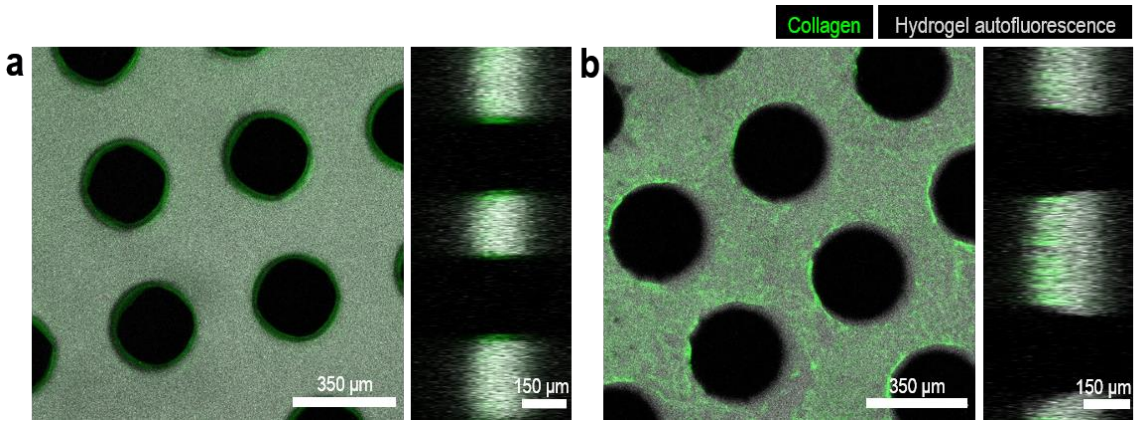

Figure 27: a) Top and cross section confocal images of the functionalized 50 seconds crypts scaffolds obtained with the Mask Aligner. b) Top and cross section confocal images of the functionalized 60 seconds crypts scaffolds obtained with the Mask Aligner.

The same problem was encountered for the deepest crypts fabricated with the Solus 3D printer. The ones that were designed with depths of 300 µm or 500 µm, when functionalized it was observed that the collagen did not arrive to the bottom, thus reducing the depth of the crypt and the surface available for the cells to attach. (Fig. 28 b)) Therefore, the effective curvature was different than the theoretical. All in all, all the fabricated crypts had a similar depth as the collagen could not penetrate further from around 120 µm. After these observations, it was hypothesized that maybe this could be avoided reducing the overexposure of the material. To do so, the concentration of tartrazine was increased to 0.05% w/v from the original bioink (section 5.4.3.). The result was that deeper crypts were achieved, but when functionalizing, once more the collagen did not reach the bottom of the structure. (Fig. 28 c)) Therefore, for the cell experiments, we used the original bioink containing 0.025% of Tartrazine and the shallowest crypts (Table 7), as in these cases the collagen completely followed the outline of the crypt (Fig. 28, panel a).

Depth	Diameter
150 µm	500 µm
150 µm	350 µm

Table 7: Summary of the sizes of the successfully functionalized crypts.

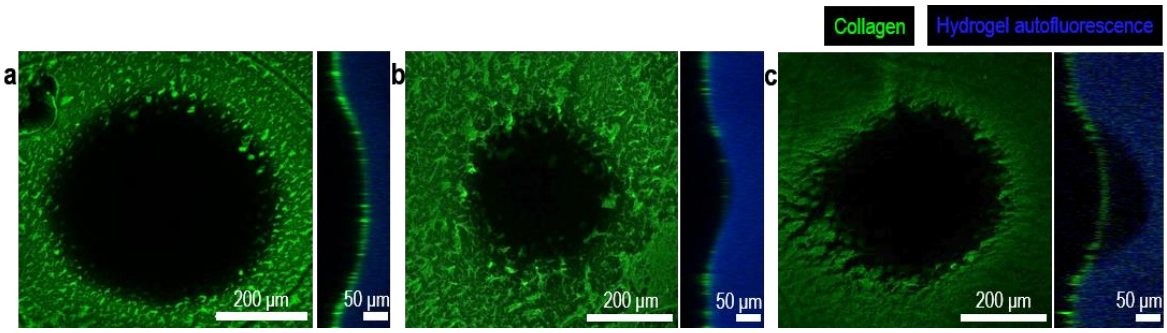

Figure 28: Confocal top and cross section images of different crypts functionalized with collagen type I. a) 500 µm diameter, 150 µm depth and bioink with 0.025% Tartrazine. The collagen perfectly follows the contour of the crypts and reaches the bottom. b) 350 µm diameter, 300 µm depth and bioink with 0.025% Tartrazine. With the increase in depth, the collagen does not reach the bottom of the crypt. c) 500 µm diameter, 150 µm depth and bioink with 0.05% Tartrazine. The doubling of Tartrazine increases the crypt depth, but the collagen does not reach the bottom of the crypt.

6.5. Curvature assessment

Once the definitive scaffolds to be used in the cell experiments were obtained, it was necessary to calculate the curvatures along the different structures. As it has been explained before, the villi and the crypts differed from the original CAD models, having a cone-shape structure instead of a cylinder. Therefore, the structures had variable radii along the vertical axis, and consequently, variable curvature, because the curvature is calculated as the inverse of the radius. Therefore, as detailed in section 5.4.10.1, the top view curvatures were measured at different points along the vertical axis of the structures. For the villi, three circles were fit (one at the top, one at the middle, and another at the base), whereas for the crypts we used two (one at the top and another at the bottom). To obtain the curvatures seen from the orthogonal cross section, another circle was fitted. The resulting curvatures after performing the necessary calculations can be seen in Fig. 29.

It can be observed how in the villi, the biggest curvatures are found at the top for all cases, which makes sense because it is where the radius of the structure is smaller. Comparing the real curvatures to the theoretical ones, it should be reminded that because the villi were modelled as a cylinder, there is one single curvature constant along the structure to compare to the three curvatures of the resulting scaffolds, and for all cases the top curvature is the one that resembles the most the theoretical one. Also, both for the orthogonal and top view curvatures, it can be seen how there is not much variability between samples, thus keeping the structures sizes from experiment to experiment.

Regarding the crypts, it is the opposite situation. It can be seen how the biggest curvature is the one at the bottom, because they are also cone-shaped structures but in the reverse order. First we find the top, which is much wider, and them the bottom where the structure is closing and the radius is smaller. However, like in the case of the villi the curvature that resembles more the theoretical one is the one at the top. For the orthogonal curvature, there are only measures of the fabricated scaffolds, because as it has been explained previously, the designs of the crypts were modeled as holes with no base, going from one side to the other of the circular disk, thus not having any curved substrate at the bottom.

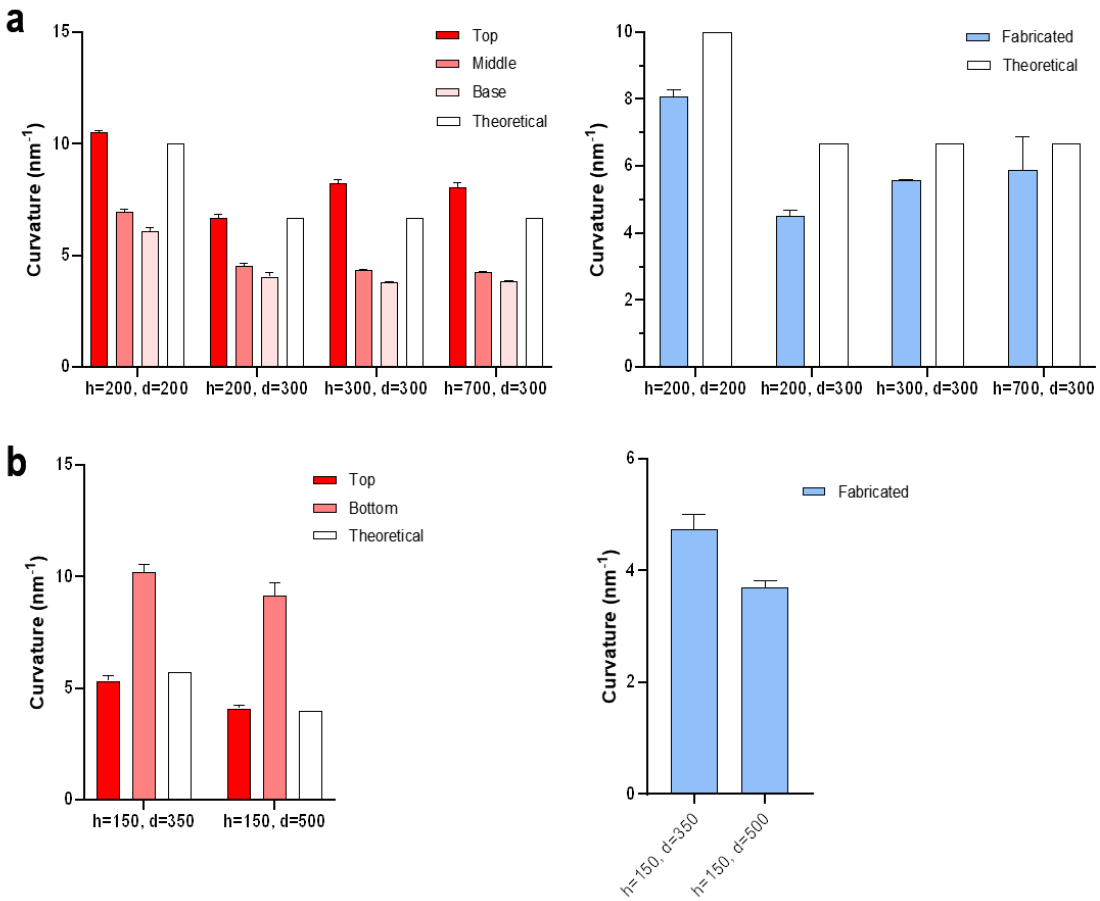

Figure 29: a) Bars plot of top view curvatures (left) and of orthogonal cross-section curvatures for different villi (right). b) Bars plot of top view curvatures (left) and of orthogonal cross-section curvatures for different crypts (right). In this case there are no comparisons with theoretical curvature because in the way the crypt models were designed they did not have orthogonal curvatures.

6.6. Cell experiments

In this section are presented the results obtained from the analysis and quantification of the images of the cells that have been seeded on the scaffolds and immunostained for different markers in order to evaluate the effect of the different curvatures on them. As said before, the cells used for these experiments are the NIH-3T3 fibroblasts (43). The fibroblasts on the scaffolds one day after the seeding can be seen in Fig. 30. The optimal cell density that was determined after some trials was 10,000 cell per scaffold.

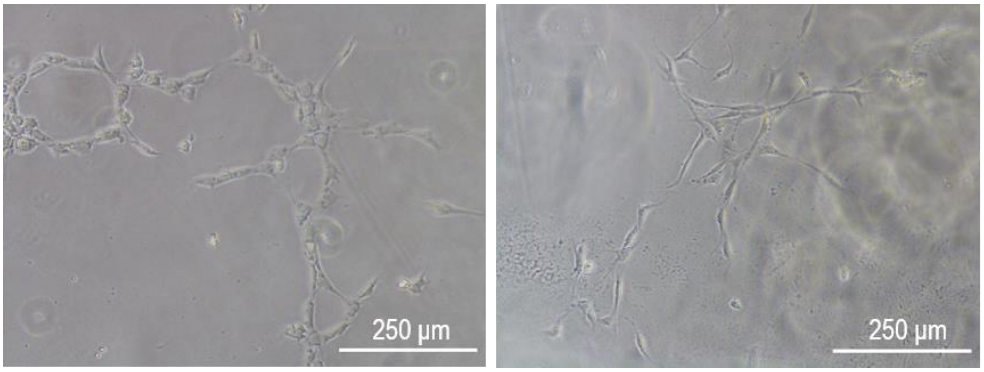

Figure 30: NIH-3T3 fibroblasts one day after being seeded on the hydrogel scaffolds.

6.6.1. Effect of curvature on fibroblasts positioning

As it has been explained before, curvature has been reported to be a cue directing cell positioning *(15)*. In this study by *Pieuchot, et al. 2018,* cells were found to accumulate mainly in concave regions, avoiding surfaces with convex curvatures. In this project, a similar effect has been observed: in the scaffolds with villi (convex curvature regions), the highest density of fibroblasts was located in the flat zone around it, and the cell concentration decreased with the increase in curvature, that is, in the base of the villi there was a higher number of fibroblasts than in the middle, whereas in turn in the middle there was a higher density compared to the top of the villi. (Fig. 31 a)) Thus, we hypothesize that once the cells were seeded on the scaffolds, they sensed the different curvatures on the regions where they located, and when they were in convex regions they migrated towards flat substrate, avoiding zones with highest curvatures.

On the other hand, in the crypt zones (concave curvature regions) cells accumulated mainly in the bottom part, even more than in the flat substrate, although at the bottom, the top view curvature was the highest. However, they probably also sensed the cross-section curvature, which was smaller, and this favored this accumulation in the bottom region. So, all in all, in crypt scaffolds the lowest cell density was in the flat regions in between the crypts, then it increased a bit on the top region of the crypts, and finally the highest concentration of fibroblasts by far was located on the base of the crypt (Fig. 31 b)).

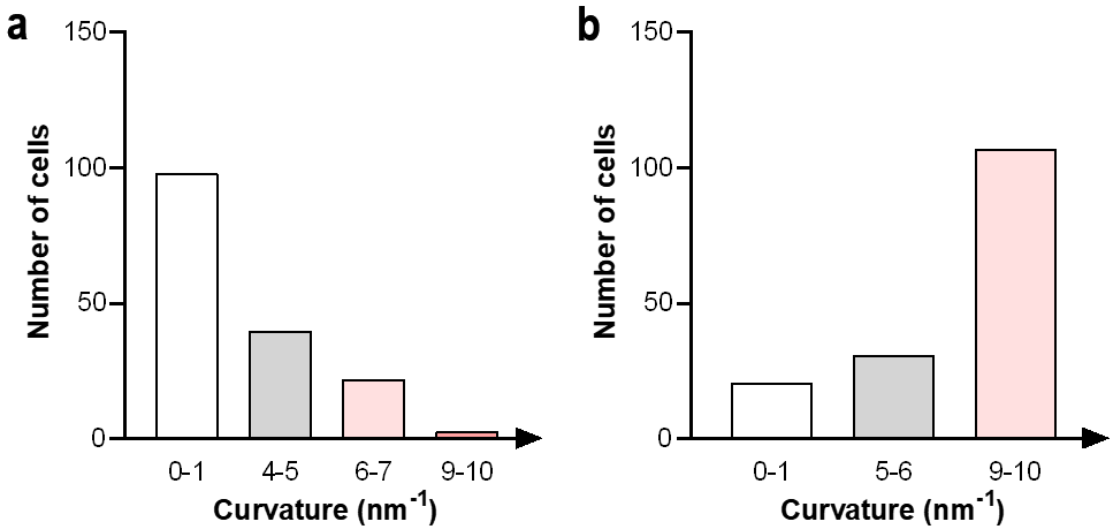

Figure 31: a) Bars plot for villi of number of cells depending on the curvature. b) Bars plot for crypts of number of cells depending on the curvature.

6.6.2. Effect of curvature on mechanosensor molecules

Yes-associated protein (YAP) is a transcriptional cofactor which when active, regulates cell proliferation and organ size by binding to TEA domain family transcription factors of the Hippo signaling pathway in the nucleus, thus being a regulator of the gene expression *(44–46)*. It also acts as a mechanosensor, being activated by mechanically stimuli, so when it is mechanically requested it is found activated in the nucleus, whereas when it is inactivated, it remains in the cytosol *(47,48)*. One example of this is the sensing of the stiffness of the ECM by epithelial cells: on soft substrates, YAP was inactive at the cytosol, whereas when increasing substrate stiffness, YAP was translocated into the nucleus becoming activated *(49)*.

The immunostainings performed on fibroblasts for this project showed a tendency of increased activation of YAP when increasing curvature. Nucleus/cytosol ratio of YAP fluorescent signal increased as curvature increased, being the maximum value on the top region of the villi and the bottom region of the crypts, the zones of maximum curvature. On the contrary, YAP was found mostly inactive in the cytosol or having a very low expression ratio on flat substrate (control). The results can be seen in the plots in Fig. 32, which have been split in crypts and villi considering that are different types of curvatures, concave and convex respectively.

These results are coherent with the ones found in the study conducted by *Mobasseri, et al. 2019*, in which they determined that for collagen-coated PDMS substrates with patterned topography, YAP was located in the nucleus of epidermal cells (keratinocytes) found in the tips of the undulations, thus showing the ability of these cells to sense the substrate curvature (50). Reinforcing these findings, in another study it was stated that convex structures act as YAP transcription activators *(51)*. According to these results, *Luciano, et al. 2021,* also found out that in MDCK epithelial cells, the nucleus/cytoplasmic YAP ratio was increased in the curved regions of the substrate, thus being activated in the nucleus, and being its maximum expression on convex curvatures *(52)*. Further, they suggested that this curvature sensing of YAP might be related to nuclear density modulation, so that YAP location would change because of cell density sensing. They determined that in low density regions, which coincided with curvature zones, YAP was in the nucleus, whereas in high cellular density areas it was located in the cytosol, which coincides with flat substrate. This hypothesis is coherent with the results that have been observed in this project for fibroblasts, being YAP activated in the villi regions, where the density of cells is lower than in the flat control substrate, in where YAP is mainly located in the cytosol and the cell density is much higher. However, it does not coincide with what we have observed in the crypts regions, where the base zone is the one having highest density of cells but still it has YAP expression in cells' nuclei. An example of fibroblasts immunostained for this marker can be seen in Fig. 33.

Also, it should be noted that YAP seems to be very sensitive to changes in curvature, because significant differences were found between almost every curvature range and its neighbor, both for the crypts and the villi, thus being able to discriminate between flat substrate and curvature but also between different ranges of curvature very close to each other, probably triggering slightly different mechanical solicitations for each case.

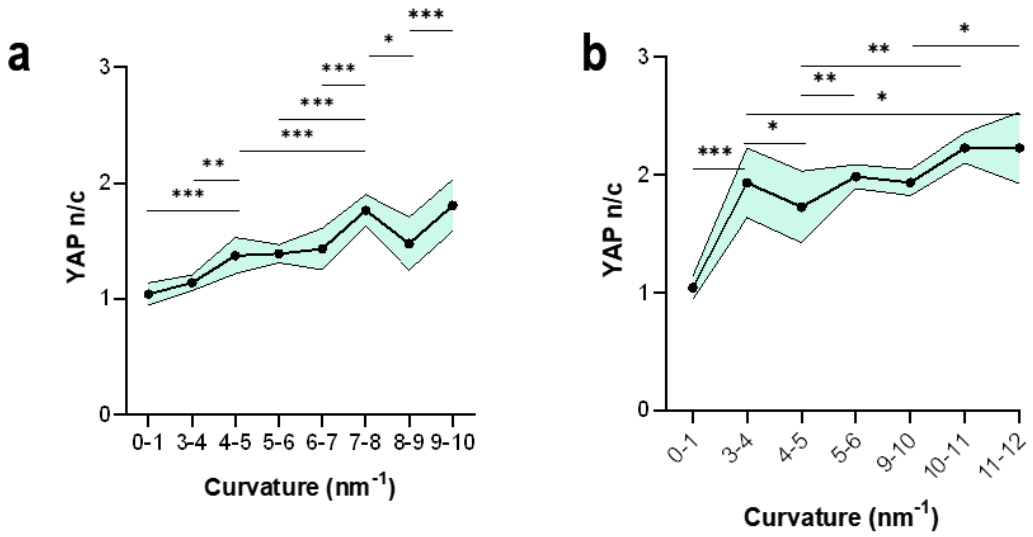

Figure 32: a) XY plot for the villi of the YAP nucleus/cytosol ratio depending on curvature representing the mean, standard deviation and significant differences. b) XY plot for the crypts of the YAP nucleus/cytosol ratio depending on curvature representing the mean, standard deviation and significant differences. For the sake of simplicity, because every curvature range was compared to each one of the rest and many statistical significances appeared, in both XY plots have only been represented the ones for each range with its closes neighbor having a significant difference.

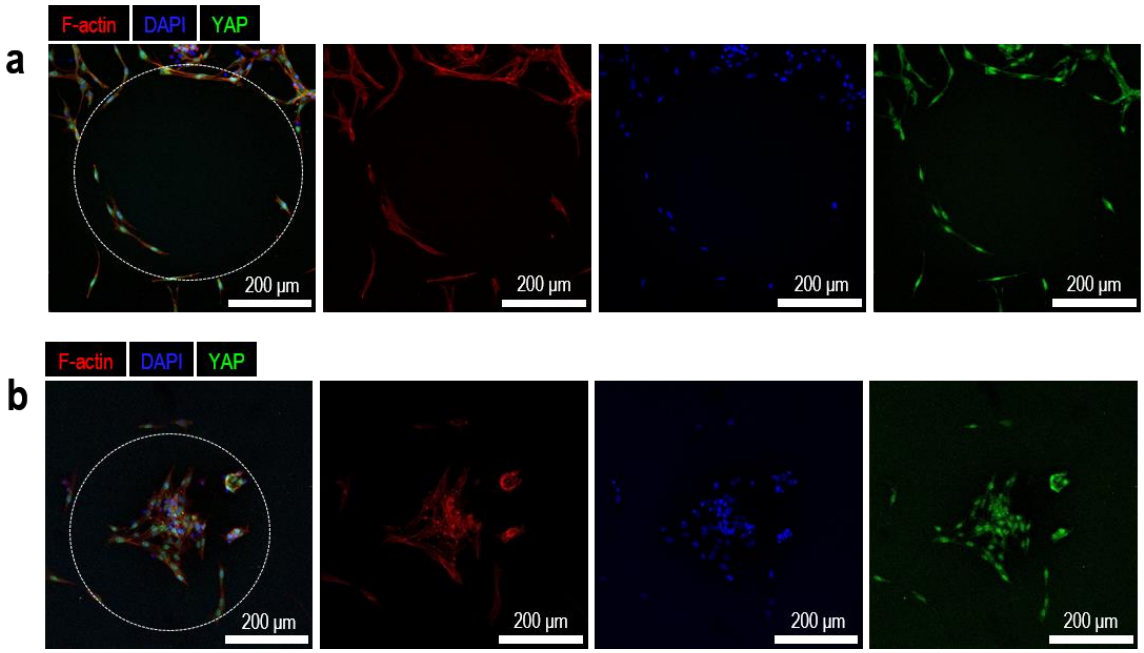

Figure 33: a) Confocal image of 3T3 fibroblasts on a 200 µm height and 300 µm diameter villi immunostained to analyze YAP expression. The white circle in the first image represents the villi. b) Confocal image of 3T3 fibroblasts on a 150 µm height and 500 µm diameter crypt immunostained to analyze YAP expression. The white circle in the first image represents the crypt.

6.6.3. Effect of curvature on extracellular matrix proteins

Laminin is one of the most widely expressed ECM proteins, exerting many important functions in multiple organs and at various developmental stages *(53)*. It is a large molecular weight glycoprotein constituted by three disulfide-linked polypeptides, forming three chains. It is indispensable for cellular networks, allowing physical bridging between the intracellular and extracellular compartments and signals critical for cellular behavior. In addition, it plays a key role in basement membranes, which are specialized ECM holding cells and tissues together, a property mainly due to their content in laminin *(54)*.

In other experiments previously performed in our lab, it has been observed that cells express different ECM proteins and in different quantities depending on where they are located. Thus, we hypothesize that this could be due to differences in substrate curvature. So, in this project it has been performed an immunostaining of the fibroblasts on the curved substrates for laminin, one of the most important ECM proteins as stated above.

Looking at the plots in Fig. 34, it can be observed an opposite tendency between crypts and villi. Whereas in the crypts regions laminin expression seems to increase as curvature increases, in the case of villi is the contrary situation: the laminin expression decreases as curvature increases. An example of fibroblasts immunostained for this marker can be seen in Fig. 35.

Although no studies have been carried out to assess these changes in secretion, following the idea of *Luciano, et al. 2021* for YAP presented in the previous section, it could be hypothesized that these changes in laminin secretion are related to cell density sensing. Indeed, there is a higher expression of laminin with increasing cell number being the lowest at the villi (minimum cellular density) and the highest at the crypts (maximum cellular density) going through the flat regions. Within the crypts, the higher the curvature (the deeper in the crypt), the higher the expression. However, within the villi, the higher the curvature, the lower the laminin expression.

Remarkably, focusing specifically on the small intestine, different ECM components were found to have a different impact on the intestinal epithelium. In particular, during gut development, the ECM is dramatically remodeled by mesenchymal cells and this is accompanied by a specific and local expression of the laminin receptor ITGA6 in the crypt-forming epithelium. In line with this, in an *in vitro* model it was found that laminin, compared to collagen type I, increased Lgr5+ stem cell and Paneth cell numbers and enabled crypt-like morphology changes *(55)*.

Finally, it should be commented that another experiment with immunostaining for fibronectin, another ECM protein, was performed, but it did not work well.

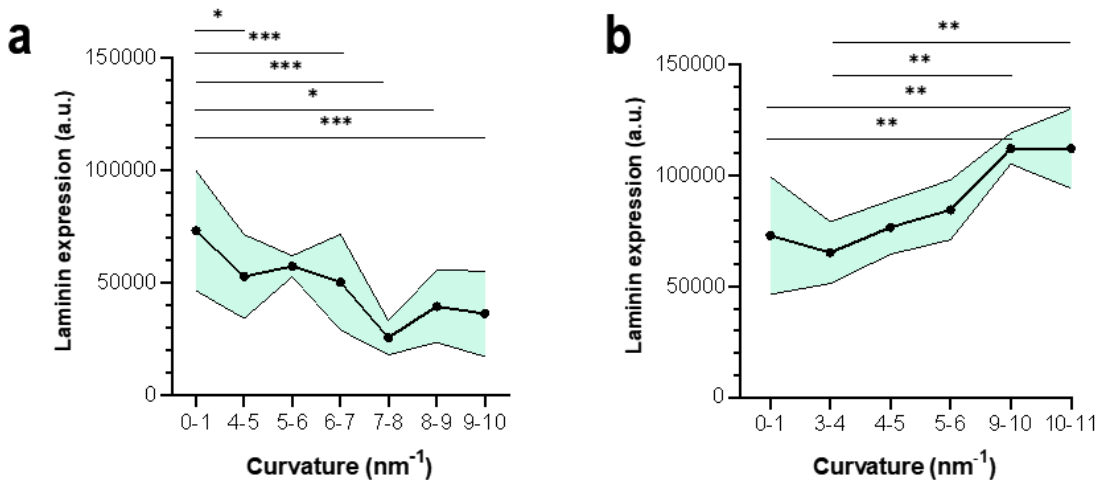

Figure 34: a) XY plot for the villi of the laminin expression depending on curvature representing the mean, standard deviation and significant differences. b) XY plot for the crypts of the laminin expression depending on curvature representing the mean, standard deviation and significant differences.

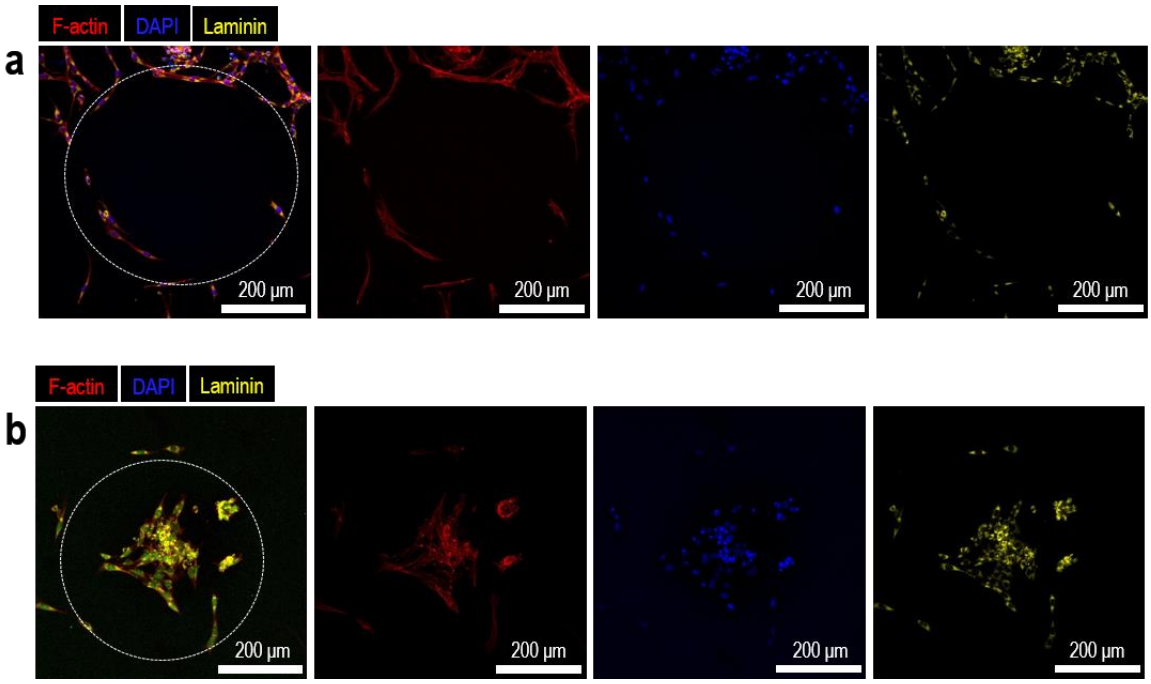

Figure 35: a) Confocal image of 3T3 fibroblasts on a 200 µm height and 300 µm diameter villi immunostained to analyze laminin expression. The white circle in the first image represents the villi. b) Confocal image of 3T3 fibroblasts on a 150 µm height and 500 µm diameter crypt immunostained to analyze laminin expression. The white circle in the first image represents the crypt.

6.6.4. Effect of curvature on cytoskeleton components

Besides mechanosensing molecules and ECM proteins, other elements that seem to be significantly impacted by substrate curvature are cytoskeleton components. In a study performed by *Pieuchot et al. 2018*, depolymerization of actin, a key component of the cytoskeleton, in cells seeded on curved substrates, leaded to a homogeneous cell distribution over the substrate, whereas when actin was intact, cells were able to sense the different curvatures and positioned according to the sensing of the distinct convexities and concavities. *(15)* So, after observing that cytoskeleton components can play a key role in curvature sensing and might be affected by topographical features, it was decided to analyze two relevant cytoskeleton elements in order to detect possible curvature-dependent changes in their expression: α-SMA and vimentin.

α-SMA is an actin isoform that contributes to cell-generated mechanical tension, mostly associated with vascular smooth muscle, but it can also be expressed in non-muscle cells such as fibroblasts and myofibroblasts *(56)*. Fibroblasts generate forces that mediate, for example, wound contraction by tractional reorganization of collagen fibers. This generation of contractile forces by fibroblasts is strongly associated with the expression of α-SMA. In myofibroblasts, α-SMA is enriched in stress fibers and focal adhesions, and it is also more abundant in actin filaments in these cells than are other actin isoforms, suggesting that this protein provides critical linkage functions between cortical actin filaments and ECM. Consequently, force transmission may be enhanced by incorporation of α-SMA into stress fibers and cortical actin filaments. Also, α-SMA expression by fibroblasts is increased by mechanical tension generated endogenously *(56).*

It has been reported that cells tend to avoid convex surfaces because they produce a higher stress on the cells, which in turn, might lead to a mechanical tension in the fibroblasts that result in a higher expression of α-SMA *(15).* The results obtained in this project seem to be consistent with these findings.

Looking at the plots in Fig. 36, it can be seen how as curvature increases, the α-SMA expression increases too for both the crypts and the villi. Furthermore, the increase in expression is higher in the villi, thus being consequent with the fact that cells suffer the highest stress on convex curvature regions, tending to avoid them *(15).* An example of fibroblasts immunostained for this marker can be seen in Fig. 37.

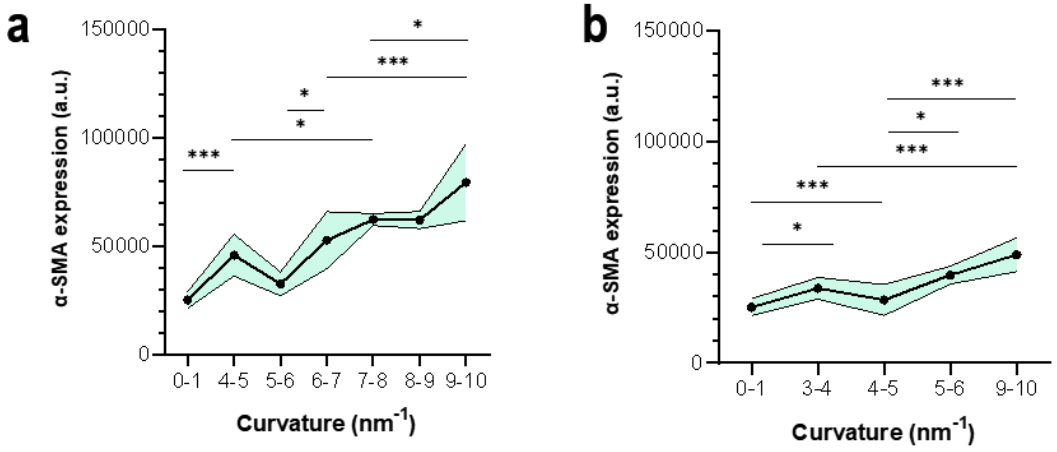

Figure 36: a) XY plot for the villi of the α-SMA expression depending on curvature representing the mean, standard

deviation and significant differences. For the sake of simplicity, because every curvature range was compared to each one of the rest and many statistical significances appeared, it has only been represented the ones for each range with its closes neighbor having a significant difference. b) XY plot for the crypts of the α-SMA expression depending on curvature representing the mean, standard deviation and significant differences.

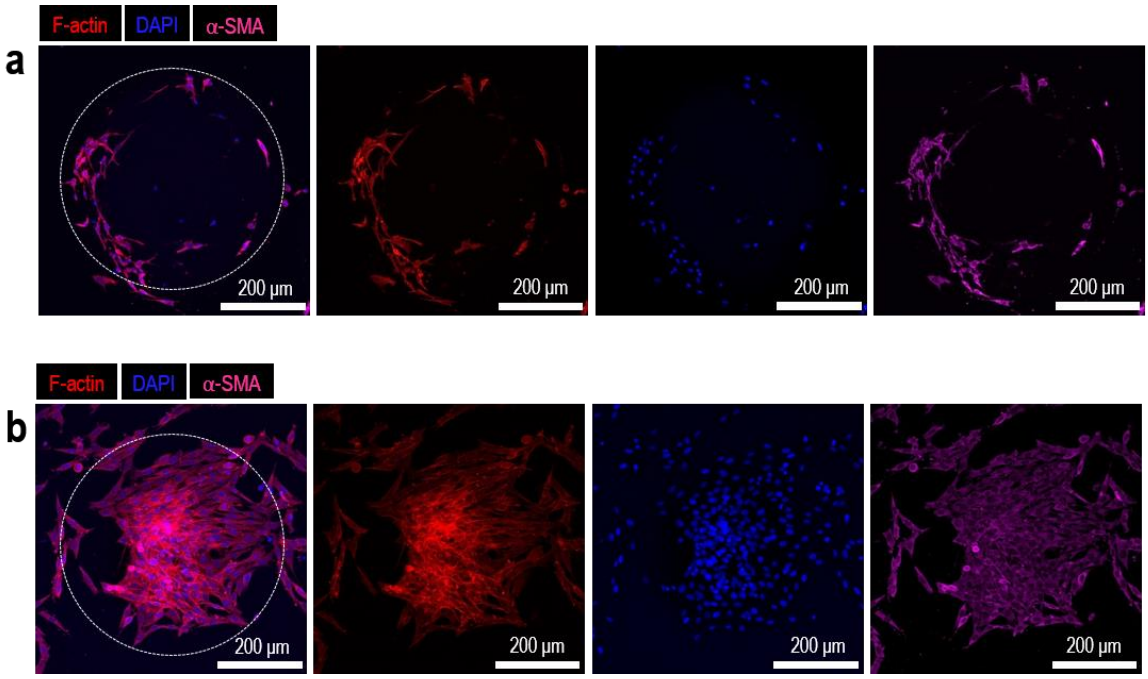

Figure 37: a) Confocal image of 3T3 fibroblasts on a 200 µm height and 300 µm diameter villi immunostained to analyze α-SMA expression. The white circle in the first image represents the villi. b) Confocal image of 3T3 fibroblasts on a 150 µm height and 500 µm diameter crypt immunostained to analyze α-SMA expression. The white circle in the first image represents the crypt.

The other cytoskeletal component analyzed was vimentin. Vimentin is a type of intermediate filament (IF) protein expressed in mesenchymal cells such as fibroblasts, among others. It plays an important role in maintaining cell integrity, polarization, and migration. It has been suggested that the vimentin level in cells affects their ability to exert force on ECM, and it is also capable of regulating cell-ECM adhesions. It contributes significantly to cell mechanics and cell traction force, and it has been suggested to be a redundant component used by cells to sense substrate stiffness (57).

Furthermore, it has been demonstrated that vimentin forms a network that provides mechanical protection of the nucleus and elasticity to the cytoskeleton. Also, vimentin IF assist in the transmission of forces to the nucleus, allowing the nucleus to better sense external forces (58). Therefore, once more the hypothesis of a higher stress leading to an increase in mechanical tension as curvature increases could be valid for the case of the villi. If convex curvature generates a higher stress on cells, this force is sensed by the fibroblasts and the vimentin expression increases. Looking at the plots in Fig. 38, there seems to be a trend in which vimentin expression increases with curvature, appearing significant differences between flat substrate and the two highest ranges of curvature (7-8 nm^{-1} and 9-10 nm^{-1}). Regarding the crypts, although the previous hypothesis would not be valid because concave curvatures promote nuclear relaxation, there

seems to be a similar trend where the vimentin expression increases with curvature, but no significant differences were found. An example of fibroblasts immunostained for this marker can be seen in Fig. 39.

However, in this experiment it has to be remarked that when inspecting the samples under the confocal microscope some variability between scaffolds was encountered. The first sample that was imaged, consisting of a villi set of different heights and diameters, had no expression at all in spite of increasing the confocal laser power at its maximum. In order to check if some mistake had been committed through the experiment, another sample containing a set of crypts was inspected, and there, although the laser power had to be increased above the limit value, vimentin was found to be expressed in the cells of that sample. Finally, it was imaged another villi scaffold to check if there might be expression only on crypts scaffolds, but then cells appeared to be expressing vimentin too. So, all in all, due to these irregularities between samples, although their immunostainings were performed all at the same time within the same process and using the same solution for each of them, just a few data could be achieved, and it was difficult to analyze the images due to the low level of intensity of the marker. Therefore, these results are not fully concluding, and the relatively small differences between curvature ranges might be due to this unaccountable variability.

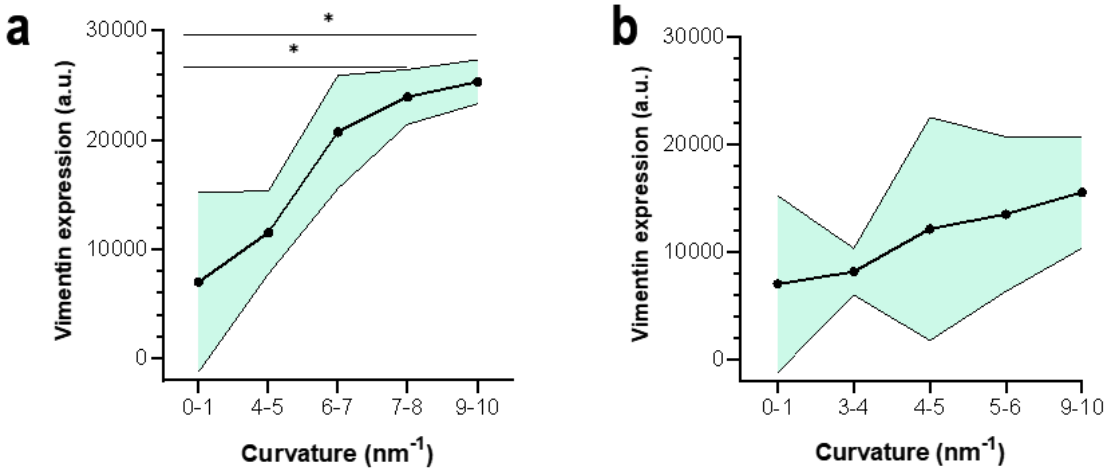

Figure 38: a) XY plot for the villi of the vimentin expression depending on curvature representing the mean, standard deviation and significant differences. b) XY plot for the crypts of the vimentin expression depending on curvature representing the mean and standard deviation. No significant differences were found in this case.

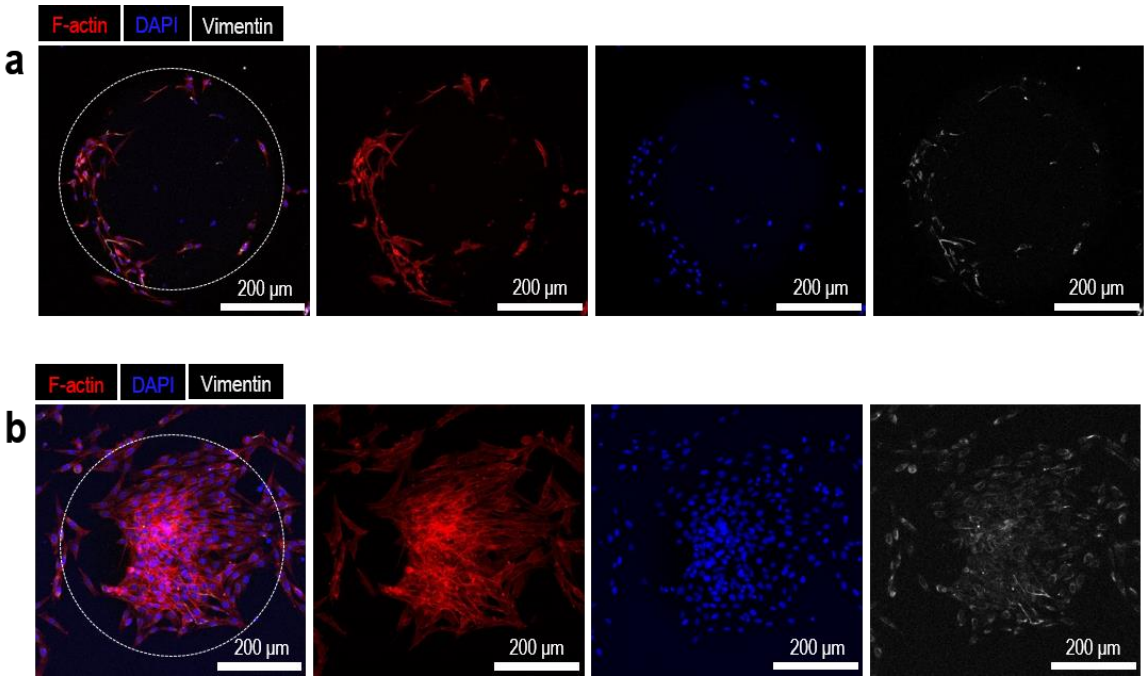

Figure 39: a) Confocal image of 3T3 fibroblasts on a 200 µm height and 300 µm diameter villi immunostained to analyze vimentin expression. The white circle in the first image represents the villi. b) Confocal image of 3T3 fibroblasts on a 150 µm height and 500 µm diameter crypt immunostained to analyze vimentin expression. The white circle in the first image represents the crypt.

7. EXECUTION SCHEDULE

7.1. Work breakdown structure (WBS)

In this section the Work Breakdown Structure (WBS) of the project is going to be detailed. (Fig. 40) Its main purpose is to organize the work into different sections or tasks to be carried out that will result in the final deliverables or accomplished objectives. The WBS, as it is defined in the Project Management Body of Knowledge, is the hierarchical decomposition of the total scope of work to be carried out by the project team to accomplish the project objectives and create the required deliverables.

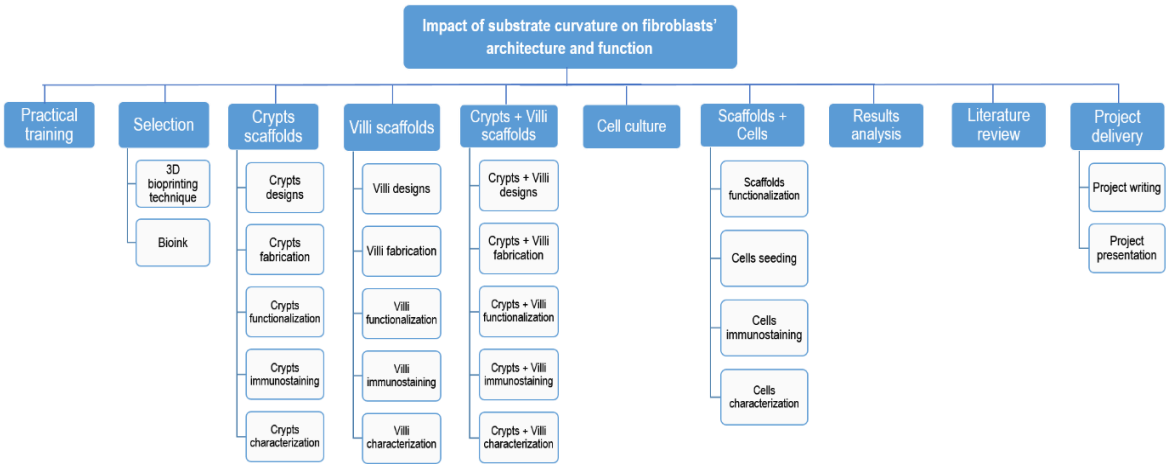

Figure 40: WBS of the project.

7.1.1. WBS Dictionary

Practical training: a training is required during the first weeks in order to learn how to use the IBEC facilities, the different available equipments and the several laboratory tasks that are needed to carry out the project like cell culture, bioprinting,... and to begin testing the materials and techniques in order to later choose the most appropriate ones.

Selection: the materials and equipment that are needed to carry out the project are chosen.

- 3D printing technique: selection of the fabrication technique of the scaffolds.
- Bioink: selection of the solution used for printing the scaffolds.
-

Crypts scaffolds: processes related with the fabrication and optimization of the printed scaffolds with crypts in order to obtain the final samples.

- Crypts designs: generation of crypts models with different diameters and depths using design software.
- Crypts fabrication: printing of the crypts scaffolds with the selected technique using the previously designed models.
- Crypts functionalization: surface modification of the scaffolds with collagen in order to optimize the attachment of antibodies for the immunostaining.

- Crypts immunostaining: attachment of the proper combination of primary and secondary antibodies to the scaffolds to later be able to visualize the fluorescence of the desired structures with confocal microscopy.
- Crypts characterization: assessment of the size of the resulting crypts with respect to the original designs and checking that the previous processes have been successful.

Villi scaffolds: processes related with the fabrication and optimization of the printed scaffolds with villi in order to obtain the final samples.

- Villi designs: generation of villi models with different diameters and heights using design software.
- Villi fabrication: printing of the villi scaffolds with the selected technique using the previously designed models.
- Villi functionalization: surface modification of the scaffolds with collagen in order to optimize the attachment of antibodies for the immunostaining.
- Villi immunostaining: attachment of the proper combination of primary and secondary antibodies to the scaffolds to be later able to visualize the fluorescence of the desired structures with confocal microscopy.
- Villi characterization: assessment of the size of the resulting villi with respect to the original designs and checking that the previous processes have been successful.

Crypts + Villi scaffolds: processes related with the fabrication and optimization of the printed scaffolds with crypts and villi together in order to obtain the final samples.

- Crypts + Villi designs: generation of crypts and villi models with different diameters, depths and heights using design software.
- Crypts + Villi fabrication: printing of the crypts and villi scaffolds with the selected technique using the previously designed models.
- Crypts + Villi functionalization: surface modification of the scaffolds with collagen in order to optimize the attachment of antibodies for the immunostaining.
- Crypts + Villi immunostaining: attachment of the proper combination of primary and secondary antibodies to the scaffolds to later be able to visualize the fluorescence of the desired structures with confocal microscopy.
- Crypts + Villi characterization: assessment of the size of the resulting crypts and villi with respect to the original designs and checking that the previous processes have been successful.

Cell culture: cell passages twice a week to maintain the cells along the duration of the project and have them available when they have to be seeded on the scaffolds to perform the curvature effect experiments.

Scaffolds + Cells: processes related to the experiments with cells to see the effect of the scaffolds' curvature on them when seeded.

- Scaffolds functionalization: surface modification of the scaffolds with collagen in order to allow the attachment of the cells to the hydrogel scaffolds.
- Cells seeding: cells are seeded on the hydrogel and left there to attach to the scaffold.

- Cells immunostaining: attachment of the proper combination of the primary and secondary antibodies to the desired markers of the cells to later be able to see the fluorescence emitted with the confocal microscopy and see the effect of the curvature on the cells with the levels of expression of the markers.
- Cells characterization: imaging of the cells in different locations of the scaffolds to evaluate the effect of the different substrate curvature on them and check if there is expression of the chosen markers or not, and at which levels.

Results analysis: the images obtained with confocal microscopy are processed, quantified and analyzed to see the different behaviors of the cells according to the changes in substrate curvature. The scaffolds' curvature is assessed with an image processing software. Finally, all the results obtained are collected and discussed.

Literature review: a bibliographic search is performed along the project to evaluate the state of the art, determine the anatomical sizes of intestinal curvatures, check the usual methods for curvature assessment, find adequate cell markers to carry out the project, and gather all the necessary background and information to perform and write the final project.

Project delivery: elaboration of the elements of the project that will be delivered for evaluation as a written report and an oral presentation.

- Project writing: a report containing all the experiments, results and necessary information of the project is written.
- Project presentation: after the delivery of the written report, an oral presentation of the project summarizing the main results and information is done in front of a thesis committee.

7.2. PERT Diagram

In this section, the Project Evaluation and Review Technique (PERT) is exposed (Fig. 41). The PERT diagram helps to estimate the duration of the project and if the times are being accomplished by calculating the length of time needed for each task of the project. Each node has the associated activity number, and an Early and a Last time to represent the duration of the activity. The lines in red represent the critical path, the set of connected activities that if it delayed the whole project will be delayed. Before elaborating the diagram, a table containing the different tasks to be done with the relations between them, the duration and the starting and ending days has been elaborated (Table 8).

ACTIVITY	NAME	PREVIOUS	NEXT	DURATION	START	ENDING
A	Practical training	-	B, F, I	23	0	23
B	Selection	A	C	1	23	24
C	Crypts scaffolds	B	D	20	24	44
D	Villi scaffolds	C	E	20	44	64
E	Crypts + Villi scaffolds	D	G, H	10	64	74
F	Cell culture	A	H	65	23	88
G	Scaffolds + Cells	E	J	25	74	99
H	Results analysis	D	J	25	84	109
I	Literature review	A	J	25	23	48
J	Project delivery	G, H, I	-	21	109	127

Table 8: Tasks matrix of the project to build the PERT diagram.

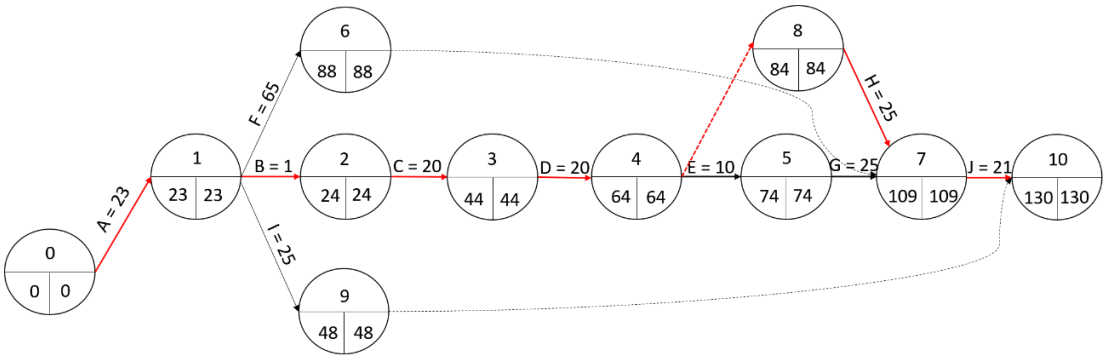

Figure 41: PERT diagram of the activities of the project.

7.3. Gantt Chart

In this section the Gantt chart is presented. (Fig. 42) This chart represents the starting and finish days of the several activities and has been elaborated taking as a base the previous task matrix and PERT diagram, except for the practical training and the selection of the technique and materials, which were performed some months before the official starting of the project experimental work, between October and December 2021.

		MONTH	FEBRUARY					MARCH					APRIL					MAY					JUNE				
		WEEK START DATE	-	7	14	21	28	7	14	21	28		4	11	18	25		2	9	16	23	30	6	13	20	27	
ACTIVITY	START DATE	END DATE	1	2	3	4	5	6	7	8	9	-	10	11	12	13	-	14	15	16	17	18	19	20	21	22	-
Literature review	07/02/2022	06/06/2022																									
Crypts scaffolds	07/02/2022	07/03/2022																									
Villi scaffolds	07/03/2022	01/04/2022																									
Crypts + Villi scaffolds	01/04/2022	11/04/2022																									
Scaffolds + Cells	11/04/2022	16/05/2022																									
Cell culture	14/02/2022	16/05/2022																									
Results analysis	25/04/2022	23/05/2022																									
Project delivery	23/05/2022	13/06/2022																									

Figure 42: Gantt chart of the activities of the project.

8. TECHNICAL FEASIBILITY

The project has been developed at the *Biomimetic Systems for Cell Engineering* group, in IBEC. All the materials, equipment and facilities needed to carry out the project were obtained either from the group laboratory or from other common facilities of IBEC, such as BioSpace (a shared space with cabinets for different purposes like cell culture), and Microscopy Characterization and MicroFab platforms.

8.1. Materials and equipment

All the materials and products used during the project were provided by the *Biomimetic Systems for Cell Engineering* group. The list of materials has been previously detailed in section 4.2. The equipments used are the following (in alphabetical order):

- Allegra X-12R centrifuge – Beckman Coulter
- BSA 124S Analytical weighing balance – Sartorius
- Centrifuge 5424R – Eppendorf
- Digital Sight DS-U3 microscope camera – Nikon
- DLP Projector – Vivitek
- ECLIPSE Ts2 optical microscope – Nikon
- Fume Hood for general use – Flores Valles
- Labculture® Class II Biological Safety Cabinet – Esco
- LSM 800 confocal microscope – ZEISS
- MJB4 Mask Aligner – SÜSS Microtech
- Moticam 3+ camera – Motic
- Polymax 1040 shaker – Heidolph Instruments
- Polytest 20 heated water bath – Fisher Scientific
- Solus 3D printer – Junction3D
- SZX10 Stereomicroscope – Olympus
- Thermo Scientific™ Forma™ Series II Water-Jacketed CO2 Incubator – Fisher Scientific
- UV Ozone ProCleaner™ – BioForce Nanosciences
- VORTEX Genius 3 – IKA

8.2. SWOT Analysis

SWOT Analysis (short for strengths, weaknesses, opportunities, threats) is a business strategy tool to assess how an organization compares to its competition. It has achieved recognition as useful in differentiating and establishing a niche within the broader market, and it can be used to analyze the internal and external strong and weak points of a project compared to the current market situation. In Table 9 it can be seen the SWOT analysis for this project.

Strengths	Weaknesses
- *In vitro* 3D model - Microstructured hydrogels fabricated through 3D bioprinting - Mimics the 3D architecture of the natural tissues Biocompatible hydrogel - Hydrogels could be fabricated by a wide range of techniques	- Premature bioprinting techniques - Limitations in resolution - Imperfect functionalization of the invaginations - Basic fibroblasts cell line
Opportunities	**Threats**
- Great market potential - Alternative to *in vivo* animal experiments - Increasing relevance and demand for 3D models - Bioprinting techniques are becoming more advanced and affordable - Impact of curvature on cell behavior is an emerging field	- Lack of specific regulations for bioprinting and its resulting products. - Early-stage research, models not scalable to industry yet. - Difficult to transition from bench to bedside, being a strictly regulated environment

Table 9: SWOT analysis of the techniques and outcomes of the project.

9. ECONOMIC VIABILITY

The *Biomimetic Systems for Cell Engineering* group has provided all the funds required for the development of this project, including the products and laboratory material and the costs of accessing to IBEC platforms. The overall costs of the project are summarized in Table 10.

For the staff, it has been considered 300 working hours and a wage of 14 €/h for the engineer carrying out the project, and 120 working hours for the supervisors and a wage of 25 €/h.

SOURCE	COST (€)
CHEMICALS AND CELLS	1013.5
LABWARE	341.3
EQUIPMENT	1727.74
SOFTWARE	-
STAFF	7200
TOTAL	**10282.54**

Table 10: Summary of all the project costs.

10. CONCLUSIONS AND FUTURE WORK

In the recent years, the translation of in vitro models from 2D to 3D has been taking increasing relevance. There have been significant advances in the technological field that allow the fabrication of microstructures in order to mimic the 3D topography of the tissues where cells usually reside. These techniques are being improved and becoming more affordable every day, rendering 3D in vitro models definitely the right alternative to improve the results obtained with 2D models. Moreover, they allow to further investigate the impact of real tissues architecture on cellular components, what is still an emerging field in which we still have a lot to learn. One clear example of the importance of tissue architecture is the effect of substrate curvature on cell behavior, which represents a more physiological environment of crucial importance in for example, tissue regeneration and pharmaceutical testing, allowing to perform drug testing in more biomimetic environments for cells than flat culture substrates.

In this project, it has been aimed to contribute to this gap of knowledge by designing and fabricating several scaffold models with different curvatures in order to assess the effect of this topographical feature on cell behavior.

After an initial step where we selected the optimal printing set-up, we stablished a procedure to obtain PEGDA-AA topographical structures with concave and convex curvatures. By using CAD designs we successfully achieved concave curvatures in the range of 100 µm – 300 µm depth and 250 µm – 500 µm diameter, and convex curvatures in the range of 200 µm – 1 mm height and 200 µm – 300 µm diameter. However, we did determine the limitations of this technique, which were below 200 µm diameter and 200 µm height.

Next, we successfully functionalized the PEGDA-AA concave and convex structures with collagen to trigger cell adhesion. Noteworthy, we have found that collagen coatings did not retrieve the shapes of concave structures deeper than 150 µm, limiting the structures suitable for cell experiments to those which had 150 µm depth and 350 µm – 500 µm diameter.

Finally, we assessed the impact of substrate curvature in NIH-3T3 fibroblasts. Our results show that: (i) fibroblasts tend to avoid convex curvatures and accumulate on flat and concave regions, (ii) YAP transcription factor translocates into the nucleus when curvature increases suggesting that cells experience different mechanical inputs in different curvatures, (iii) the cytoskeleton components α-SMA and vimentin are more expressed when curvature is increased as well, reinforcing the idea of changes in cell's mechanical state depending on substrate curvature, and (iv) cells expressed more ECM protein laminin on concave curvatures than on convex ones.

Altogether we have shown that indeed evaginations (convex structures) and invaginations (concave structures), like the ones found in intestinal tissue in vivo, alter cell positioning, cytoskeleton organization, transcription factors localization and protein secretion. This results are in line with the initial hypothesis of the project, which should now be tested with a more relevant cell line.

After all these highlights of the project results, it should be remarked that there is still a lot of road ahead to improve these 3D *in vitro* models, as well as there is a need to perform more experiments not only to validate these results but also to further investigate the effects of substrate curvature on different cell types. In this project, the experiments have been carried out with a basic fibroblasts cell line as a preliminary study to assess if the fabricated substrates with their curvatures are able to trigger a cell response. As we have observed that these substrate curvatures have a high impact on many cellular processes, we believe it would be interesting to perform further studies with more complex cell types such as primary intestinal fibroblasts. On the other hand, throughout this project we have encountered some issues that need to be addressed such as the difficulty of functionalizing the bottom of the deepest invaginations tested. This projected has also unveiled the limitations of the fabrication technique used, the resolution not allowing to print thinner structures which would otherwise have enabled to test a higher range of curvatures. Nevertheless, despite the great room for improvement, our developed *in vitro* 3D curved models have been able to trigger different cellular responses in distinct curvature ranges, which have been achieved by means of a relatively simple and fast process, and without showing significant variations from batch to batch, thus allowing reproducibility for further experiments. So, all in all, 3D models mimicking real topographical features are here to stay considering all the advantages they have compared to traditional models.

REFERENCES

1. Kimchi ET, Gusani NJ, Kaifi JT. Anatomy and physiology of the small intestine. Eighth Edi. Greenfield's Surgery: Scientific Principles and Practice: Fifth Edition. Elsevier Inc.; 2012. 737–748 p. https://doi.org/10.1016/B978-0-323-40232-3.00071-6

2. Castaño AG, García-Díaz M, Torras N, Altay G, Comelles J, Martínez E. Dynamic photopolymerization produces complex microstructures on hydrogels in a moldless approach to generate a 3D intestinal tissue model. Biofabrication. 2019;11(2).

3. Marsh MN, Swift JA. A study of the small intestinal mucosa using the scanning electron microscope. Gut. 1969;10(11):940–9.

4. Sumigray KD, Terwilliger M, Lechler T. Morphogenesis and Compartmentalization of the Intestinal Crypt. Dev Cell. 2018;45(2):183-197.e5.https://doi.org/10.1016/j.devcel.2018.03.024

5. Noah TK, Donahue B, Shroyer NF. Intestinal development and differentiation. Exp Cell Res. 2011;317(19):2702–10.: http://dx.doi.org/10.1016/j.yexcr.2011.09.006

6. Lei NY, Jabaji Z, Wang J, Joshi VS, Brinkley GJ, Khalil H, et al. Intestinal subepithelial myofibroblasts support the growth of intestinal epithelial stem cells. PLoS One. 2014;9(1).

7. Lee J, Abdeen AA, Wycislo KL, Fan TM, Kilian KA. Interfacial geometry dictates cancer cell tumorigenicity. Nat Mater. 2016;15(8):856–62.

8. Yu SM, Oh JM, Lee J, Lee-Kwon W, Jung W, Amblard F, et al. Substrate curvature affects the shape, orientation, and polarization of renal epithelial cells. Acta Biomater. 2018;77:311–21. https://doi.org/10.1016/j.actbio.2018.07.019

9. Huang G, Wang L, Wang S, Han Y, Wu J, Zhang Q, et al. Engineering three-dimensional cell mechanical microenvironment with hydrogels. Biofabrication. 2012;4(4).

10. Santos E, Hernández RM, Pedraz JL, Orive G. Novel advances in the design of three-dimensional bio-scaffolds to control cell fate: Translation from 2D to 3D. Trends Biotechnol. 2012;30(6):331–41.

11. Cukierman E, Pankov R, Stevens DR, Yamada KM. Taking cell-matrix adhesions to the third dimension. Science (80-). 2001;294(5547):1708–12.

12. Sung JH, Yu J, Luo D, Shuler ML, March JC. Microscale 3-D hydrogel scaffold for biomimetic gastrointestinal (GI) tract model. Lab Chip. 2011;11(3):389–92.

13. Taebnia N, Zhang R, Kromann EB, Dolatshahi-Pirouz A, Andresen TL, Larsen NB. Dual-Material 3D-Printed Intestinal Model Devices with Integrated Villi-like Scaffolds. ACS Appl Mater Interfaces. 2021;13(49):58434–46.

14. Agarwal T, Onesto V, Lamboni L, Ansari A, Maiti TK, Makvandi P, et al. Engineering biomimetic intestinal topological features in 3D tissue models: retrospects and prospects. Bio-Design Manuf. 2021;4(3):568–95. https://doi.org/10.1007/s42242-020-00120-5

15. Pieuchot L, Marteau J, Guignandon A, Dos Santos T, Brigaud I, Chauvy PF, et al. Curvotaxis directs cell migration through cell-scale curvature landscapes. Nat Commun. 2018;9(1).

16. Bade ND, Kamien RD, Assoian RK, Stebe KJ. Curvature and Rho activation differentially control the alignment of cells and stress fibers. Sci Adv. 2017;3(9):1–9.

17. Bade ND, Xu T, Kamien RD, Assoian RK, Stebe KJ. Gaussian Curvature Directs Stress Fiber Orientation and Cell Migration. Biophys J. 2018;114(6):1467–76. https://doi.org/10.1016/j.bpj.2018.01.039

18. Lee SJ, Yang S. Substrate Curvature Restricts Spreading and Induces Differentiation of Human Mesenchymal Stem Cells. Biotechnol J. 2017;12(9):1–10.

19. Sia J, Yu P, Srivastava D, Li S. Effect of biophysical cues on reprogramming to cardiomyocytes. Biomaterials. 2016;103:1–11. http://dx.doi.org/10.1016/j.biomaterials.2016.06.034

20. Wang Y, Gunasekara DB, Reed MI, DiSalvo M, Bultman SJ, Sims CE, et al. A microengineered collagen scaffold for generating a polarized crypt-villus architecture of human small intestinal epithelium. Biomaterials. 2017;128:44–55. http://dx.doi.org/10.1016/j.biomaterials.2017.03.005

21. Ladd MR, Costello CM, Gosztyla C, Werts AD, Johnson B, Fulton WB, et al. Development of Intestinal Scaffolds that Mimic Native Mammalian Intestinal Tissue. Tissue Eng - Part A. 2019;25(17–18):1225–41.

22. Vedadghavami A, Minooei F, Mohammadi MH, Khetani S, Rezaei Kolahchi A, Mashayekhan S, et al. Manufacturing of hydrogel biomaterials with controlled mechanical properties for tissue engineering applications. Acta Biomater. 2017;62:42–63. https://doi.org/10.1016/j.actbio.2017.07.028

23. Molley TG, Wang X, Hung T tyng, Jayathilaka PB, Yang JL, Kilian KA. Geometrically Structured Microtumors in 3D Hydrogel Matrices. Adv Biosyst. 2020;4(5):1–8.

24. Zhu Y, Fan R, Zheng Z, Zhu Z, Si T, Xu RX. Preparation of Anisotropic Micro-Hydrogels with Tunable Structural and Topographic Features by Compound Interfacial Shearing. ACS Appl Mater Interfaces. 2021;13(35):42114–24.

25. Ramiah P, du Toit LC, Choonara YE, Kondiah PPD, Pillay V. Hydrogel-Based Bioinks for 3D Bioprinting in Tissue Regeneration. Front Mater. 2020;7(April):1–13.

26. Mancha Sánchez E, Gómez-Blanco JC, López Nieto E, Casado JG, Macías-García A, Díaz Díez MA, et al. Hydrogels for Bioprinting: A Systematic Review of Hydrogels Synthesis, Bioprinting Parameters, and Bioprinted Structures Behavior. Front Bioeng Biotechnol. 2020;8(August).

27. Ru Choi J, Yong KW, Cowie AC. Recent advances in photo-crosslinkable hydrogels for biomedical applications. Biotechniques. 2019;66(1):40–53.

28. Ding C, Chen X, Kang Q, Yan X. Biomedical Application of Functional Materials in Organ-on-a-Chip. Front Bioeng Biotechnol. 2020;8(July):1–9.

29. Gungor-Ozkerim PS, Inci I, Zhang YS, Khademhosseini A, Dokmeci MR. Bioinks for 3D bioprinting: An overview. Biomater Sci. 2018;6(5):915–46.

30. Heinrich MA, Liu W, Jimenez A, Yang J, Akpek A, Liu X, et al. 3D Bioprinting: from Benches to Translational Applications. Small. 2019;15(23):1–88.

31. He Y, Gu Z, Xie M, Fu J, Lin H. Why choose 3D bioprinting? Part II: methods and bioprinters. Bio-Design Manuf. 2020;3(1):1–4. https://doi.org/10.1007/s42242-020-00064-w

32. Gu Z, Fu J, Lin H, He Y. Development of 3D bioprinting: From printing methods to biomedical applications. Asian J Pharm Sci. 2020;15(5):529–57. https://doi.org/10.1016/j.ajps.2019.11.003

33. Liang R, Gu Y, Wu Y, Bunpetch V, Zhang S. Lithography-Based 3D Bioprinting and Bioinks for Bone Repair and Regeneration. ACS Biomater Sci Eng. 2021;7(3):806–16.

34. Kelly E. FDA regulation of 3D-printed organs and associated ethical challenges. Univ PA Law Rev. 2018;166(2):515–45.

35. Wu MH, Huang S Bin, Lee G Bin. Microfluidic cell culture systems for drug research. Lab Chip. 2010;10(8):939–56.

36. Description P, Responses MS, Outcomes P, Engineering BI, Ingber DE. Organs-On-Chips for Radiation Countermeasures Update : Modeling Sex-Specific Responses. 2019;(September 2013):1–5.

37. Vives J, Batlle-Morera L. The challenge of developing human 3D organoids into medicines. Stem Cell Res Ther. 2020;11(1):1–4.

38. Kritikos M. 3D bio-printing for medical and enhancement purposes: Legal and ethical aspects. Eur Parliam. 2018; http://www.europarl.europa.eu/RegData/etudes/IDAN/2018/614571/EPRS_IDA(2018)614571(ANN2)_EN.pdf

39. Placone JK, Engler AJ. Recent Advances in Extrusion-Based 3D Printing for Biomedical Applications. Adv Healthc Mater. 2018;7(8):1–11.

40. Yang W, Yu H, Liang W, Wang Y, Liu L. Rapid fabrication of hydrogel microstructures using UV-induced projection printing. Micromachines. 2015;6(12):1903–13.

41. Vila A, Torras N, Castaño AG, García-Díaz M, Comelles J, Pérez-Berezo T, et al. Hydrogel co-networks of gelatine methacrylate and poly(ethylene glycol) diacrylate sustain 3D functional in vitro models of intestinal mucosa. Biofabrication. 2019;12:1–16.

42. Frantz C, Stewart KM, Weaver VM. The extracellular matrix at a glance. J Cell Sci. 2010;123(24):4195–200.

43. Szabó P, Kolář M, Dvořánková B, Lacina L, Štork J, Vlček Č, et al. Mouse 3T3 fibroblasts under the influence of fibroblasts isolated from stroma of human basal cell carcinoma acquire properties of multipotent stem cells. Biol Cell. 2011;103(5):233–48.

44. Sunaga S, Kofuji S, Nishina H. YAP drives cell competition by activating choline metabolism. Biochem Biophys Res Commun. 2021;572:178–84. https://doi.org/10.1016/j.bbrc.2021.07.101

45. JIANG L, LI J, ZHANG C, SHANG Y, LIN J. YAP-mediated crosstalk between the Wnt and Hippo signaling pathways (Review). Mol Med Rep. 2020;22(5):4101–6.

46. Pan X, Wu B, Fan X, Xu G, Ou C, Chen M. YAP accelerates vascular senescence via blocking autophagic flux and activating mTOR. J Cell Mol Med. 2021;25(1):170–83.

47. Calvo F, Ege N, Grande-Garcia A, Hooper S, Jenkins RP, Chaudhry SI, et al. Mechanotransduction and YAP-dependent matrix remodelling is required for the generation and maintenance of cancer-associated fibroblasts. Nat Cell Biol. 2013;15(6):637–46.

48. Maller O, Dufort CC, Weaver VM. YAP forces fibroblasts to feel the tension. Nat Cell Biol. 2013;15(6):570–2.

49. Dupont S, Morsut L, Aragona M, Enzo E, Giulitti S, Cordenonsi M, et al. Role of YAP/TAZ in mechanotransduction. Nature. 2011;474(7350):179–84.

50. Mobasseri SA, Zijl S, Salameti V, Walko G, Stannard A, Garcia-Manyes S, et al. Patterning of human epidermal stem cells on undulating elastomer substrates reflects differences in cell stiffness. Acta Biomater. 2019;87:256–64. https://doi.org/10.1016/j.actbio.2019.01.063

51. Baptista D, Teixeira L, van Blitterswijk C, Giselbrecht S, Truckenmüller R. Overlooked? Underestimated? Effects of Substrate Curvature on Cell Behavior. Trends Biotechnol. 2019;37(8):838–54. https://doi.org/10.1016/j.tibtech.2019.01.006

52. Luciano M, Xue S, Vos WH De, Redondo-morata L, Surin M, Lafont F, et al. Cell monolayers sense curvature by exploiting active mechanics and nuclear mechanoadaptation.

53. Yao Y. Laminin: loss-of-function studies. Cell Mol Life Sci. 2017;74(6):1095–115.

54. Aumailley M. The laminin family. Cell Adhes Migr. 2013;7(1):48–55.

55. Neerven V, Garcia M. The extracellular matrix controls stem cell specification and tissue morphology in the developing and adult gut. bioRxiv. 2021;2021.04.14.439776. https://doi.org/10.1101/2021.04.14.439776

56. Wang J, Zohar R, McCulloch CA. Multiple roles of α-smooth muscle actin in mechanotransduction. Exp Cell Res. 2006;312(3):205–14.

57. Ho Thanh MT, Grella A, Kole D, Ambady S, Wen Q. Vimentin intermediate filaments modulate cell traction force but not cell sensitivity to substrate stiffness. Cytoskeleton. 2021;78(6):293–302.

58. Patteson AE, Vahabikashi A, Goldman RD, Janmey PA. Mechanical and Non-Mechanical Functions of Filamentous and Non-Filamentous Vimentin. BioEssays. 2020;42(11):1–12.